Upscaling poromechanical models of coalbed methane reservoir incorporating the interplay between non-linear cleat deformation and solvation forces

Quoc Ha, Tien Dung Le, Irina Panfilov, Christian Moyne, Marcio Murad

Upscaling Poromechanical Models of Coalbed Methane Reservoir Incorporating the Interplay between Non-linear Cleat Deformation and Solvation Forces

Quoc D. Ha [1], Tien D. Le[1], Irina Panfilov[1], Christian Moyne[1] Marcio A. Murad[2]

[1] LEMTA, University of Lorraine, CNRS,Nancy, France

[2] LNCC, Laboratório Nacional de Computacao Cientifica, Petrópolis, RJ, Brazil

e-mail: quoc-dat.ha@univ-lorraine.fr, tien-dung.le@univ-lorraine.fr,

irina.panfilova@univ-lorraine.fr, christian.moyne@univ-lorraine.fr,

murad@lncc.br

March 1, 2023

Abstract

We construct herein a three-scale coupled mechanical model for naturally fractured coalbed methane reservoir with the ability of describing the stress balance between the solvation force, arising from the gas adsorption in nanopores, and the restoration stress stemming from the elastic response of the cleats. To determine the cleat porosity, the non-linear hyperbolic Barton-Bandis (BB) law, which captures increase in joint stiffness induced by the cleat closure due to matrix swelling, is postulated for the fracture mechanical response. At the microscale, the theory incorporates the coupling between the effects of the solvation force and the elastic response of the

matrix. Such system of governing equations is coupled with the fluid pressure in the discrete cleat system with dependency of aperture with the normal stress dictated by the aforementioned BB-model. A reiterated homogenized procedure is pursued and capable of providing the constitutive response of the homogenized poromechanical parameters on gas pressure. Numerical simulations illustrate the performance of the proposed model.

keywords: Three-scale poromechanical model; Enhanced Coalbed Methane Recovery; Non-linear Barton-Bandis law; Adsorption effects

1 Introduction

It has been well documented that gradual increase of carbon dioxide concentration in the atmosphere induces global warming. Several procedures, commonly adopted to mitigate such an undesirable phenomenon, consist in the long-term storage of supercritical CO_2 in underground geological sites, such as active or depleted oil and gas fields, deep saline aquifers, methane hydrate formations, coal seams and salt caverns [1, 2, 3]. Among the aforementioned sequestration scenarios, we are particularly interested in the enhanced coalbed methane recovery (ECBMR) in unmineable coal seams combined with CO_2 sequestration [4, 5, 6, 7, 8, 9]. Such an attractive combination is motivated by the large quantities of sorbed methane in coal, combined with the high capacity of the coal matrix for storing large amounts of carbon dioxide and consequently generating revenue that mitigates the expenses of sequestration [4, 5]. In coalbed methane reservoirs, the primary production stage is dictated by traditional pressure drawdown which induces methane desorption from the nanopores, with subsequent diffusion in the matrix and flow through the higher permeability layers (cleats) toward the production wells [4, 10]. Owing to the higher affinity with the solid phase, particularly higher adsorption capacity, injected CO_2 maintains the reservoir pressure but decreases the partial pressure of methane causing desorption from the surfaces of the coal matrix. In addition, subsequently CO_2 displaces methane

towards the production wells enhancing gas production [4, 5].

Fractured coalbed matrix consists of a canonical example of a system characterized by a bimodal structure with two distinct porous systems commonly referred to as cleat (natural fracture) and matrix. The former is associated with the gas (and water) percolation whereas the latter dominates the storativity along with slow diffusion within the matrix [4]. Owing to the molecular nature of adsorption, the description requires the use of discrete models or intermediate statistical mechanics tools. Moreover, multiscale flow and diffusion patterns are ruled by phenomena described in terms of continuum physics at two coarser natural scales associated with the expansive matrix intertwined by the cleat system (micro), and the entire macroscopic picture of the homogenized system (macro) characterized by juxtaposed different continua (see Figure 1).

A peculiar feature regarding coalbed methane reservoir modeling is the necessity of introducing hydro-mechanical coupled phenomena in order to describe, in an accurate manner, the evolution of the cumulative production curves along with the performance of injector wells [11, 7, 8]. In this context, inclusion of matrix swelling containing nanopores is of utmost importance and appears strongly correlated with the anomalous behavior of the confined fluid [12, 13]. In such a context, it becomes mandatory to develop an accurate description of the fluid-solid intermolecular interaction with the ability to capture local adsorption in the vicinity of the nanopore walls in conjunction with efficient up-scaling methods to propagate the local information to the macroscopic scale. In a sequence of papers [14, 15, 16], the authors have combined the Density Functional Theory (DFT) with formal homogenization methods to derive three-scale methods for expansive porous media containing nanopores and natural fractures. More specifically in [15] the authors constructed a new three-scale geomechanical approach for an anomalous mixture of gases in nanopores with spherical geometry coupled with a cleat system of totally open fractures with zero traction on the boundary. In addition to the strong fluid-solid interaction within the coal matrix, competitive mechanisms between desorption induced swelling and the restoring incremental elastic stress due to the mechanical interaction between

opposite cleat asperities tend to provide asymptotic stable values of cleat porosity and permeability [12, 17, 15, 14]. Thus, understanding and quantifying accurately the gas-matrix-cleat interactions are crucial for reliable long-term predictions of methane withdrawal and carbon dioxide retention in coal seams.

A particular feature of jointed rocks lies in the description of the non-linear stresses induced by the progressive contact between opposite rough-walled surfaces [18, 19, 20]. In this setting, the underlying fine-scale model must have the ability to incorporate the constitutive response of normal and tangential stresses of the joint network, which are strongly dependent on joint closure. The mutual mechanical contact between adjacent asperities in opposite faces gives rise to enhancement in joint stiffness as the gap progressively moves towards the range of very small apertures. Such a non-linear elastic response has been reported in the literature as a cornerstone of a general model commonly referred to as Barton-Bandis model [21, 19]. In this context, the joint-normal stress behaves in a hyperbolic fashion with the displacement jump, whereas the shear component exhibits a quasi-linear dependence on the tangential jump up to a peak, where strong softening inelastic behavior followed by dilatancy takes place [22].

In this work, our goal consists in the development of a three-scale poromechanical model with capabilities of capturing the interplay between matrix swelling and non-linear cleat restoring force dictated by the Barton-Bandis law. In order to accomplish this task, we begin by constructing the two-scale poromechanical model for the expansive matrix by combining the results obtained with the DFT for the solvation force with a formal homogenization of an elastic matrix perforated by nanopores saturated by an anomalous adsorbed gas. Such an upscaling provides incremental constitutive laws with additional features such as pore pressure dependency of the elastic modulus and Biot-Willis coefficient stemming from the solvation force. Subsequently, we proceed within the context of a reiterated homogenization procedure [23, 24] in the sense of [25, 26, 27] to incorporate discontinuities inherent to the cleat network ruled by the non-linear constitutive law of Barton-Bandis type giving

rise to a three-scale homogenized incremental poromechanical model. A remarkable consequence of the three-scale approach relies in the construction of the local closure problems for the effective parameters in the incremental laws, whose solution provides the underlying characteristic function profiles. Unlike previous work [14, 15, 16], the new closure problems show ability to capture the interplay between solvation forces and the corresponding counter force in the cleat system dictated by the non-linear elastic law.

Numerical results illustrate the evolution of cleat closure and poromechanical parameters in an example of CO_2 sequestration in a box-shaped reservoir with a prescribed pore pressure evolution, highlighting the potential of the new model proposed herein.

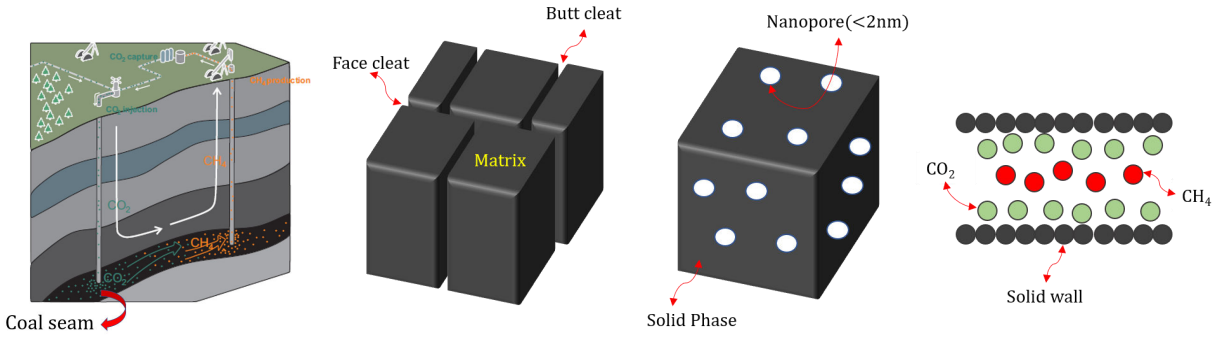

(a) Macroscale [28] O(m) (b) Microscale O(mm) (c) Nanoscale O(nm) (d) Molecular scale O(nm)

Figure 1: Natural length scales of a coalbed methane reservoir

2 Review of the Constitutive Laws at the Different Scales

We consider a mixture of gases (CH_4 and CO_2) in a coal seam characterized by a bimodal structure composed of nanopores within the matrix intertwined by a discrete periodic network of cleats. The gases are thermodynamically adsorbed within the nanopores. The coal skeleton is assumed elastic and submitted to a stress field induced by solvation forces stemming from intermolecular interactions between gas molecules and the walls of the nanopore system. Such a mechanical interaction induces

swelling/shrinking of the coal skeleton which gives rise to mechanical perturbations in the fracture aperture consequently modifying cleat permeability. The cleat network is treated as a lower $n-1$-dimensional object for $n = 2, 3$ with the constitutive response of the averaged normal and tangential stresses ruled by the non-linear hyperbolic law postulated by Barton and Bandis (BB) [19, 22, 29, 21].

For the sake of completeness, we begin by reviewing the underlying constitutive response of the poromechanical variables considered in our subsequent developments, namely the solvation force induced by the adsorption and the restoring non-linear BB law for the cleats.

2.1 Solvation force

Our nanoscopic picture consists of a confined mixture of N_g gases distributed in a heterogeneous fashion in nanopores in equilibrium with an outer bulk solution. Unlike bulk fluids, confined gases commonly exhibit anomalous behavior in nanopores [16]. In this setting the solid surfaces of the nanopores interact with the gas molecules through a prescribed Lennard-Jones potential, repulsive and attractive at short and long distances respectively [30]. Such an interaction induces a stress field in the fluid $\boldsymbol{\sigma}_n$. In order to compute its distribution in the nanopores, we begin by denoting Ω_n the sub-domain occupied by the heterogeneous gas (see Figure 2), in which under absence of gravitational forces satisfies the local equilibrium

$$\boldsymbol{\nabla} \cdot \boldsymbol{\sigma}_n = 0 \qquad \text{in } \Omega_n \tag{1}$$

In addition, at the solid/fluid interface Γ_{ns}, by invoking the definition of the solvation force $\boldsymbol{\Pi}$ exerted on the solid surface by the confined fluids, as an excess quantity with respect to a reference pressure p_m associated with the non-perturbed bulk state, continuity of the traction reads as

$$\boldsymbol{\sigma}_n \cdot \mathbf{n} = -\left(\boldsymbol{\Pi} + p_m \mathbf{n}\right) \quad \text{on } \Gamma_{ns} \tag{2}$$

where **n** is the unit normal pointing outward to the sub-domain occupied by the fluid phase.

For the sake of completeness, we proceed straightforward from our previous Density Functional Theory-based framework constructed in [16]. In such a thermodynamically based context applied to a pore of arbitrary geometry, by postulating proper representation of the grand potential along with fluid-fluid and fluid-solid Lennard-Jones based potentials in the grand canonical ensemble, the derivatives with respect to changes in pore volume furnish the solvation force. In should be noted that due to the complex nanopore geometry (see Figure 2 for example), the distribution of the solvation force can be non-uniform on the solid wall.

To illustrate the numerical outcome of this methodology, let consider a fluid (CO_2) confined in a spherical nanopore of radius $R_p = 2.5\, d_{CO_2}$ where d_{CO_2} refers to the diameter of the CO_2 molecule. Figures 3(a) and (b) show the variation of the solvation force as a function of the CO_2 bulk pressure and the radial distribution function for three values of the CO_2 bulk pressure denoted by A, B, C. It should be noted that, owing to the adsorption of gas molecules at the vicinity of the solid surface, the solvation force tends to "pull" the pore wall acting as a traction in the direction to close the nanopores. This yields a negative value of Π with $\mathbf{\Pi} = \Pi\mathbf{n}$ in (2) with a magnitude much higher than the bulk pressure. More specifically, at low CO_2 pressures, the gas molecules tend to move towards the attractive zone inside the nanopores, located in the vicinity of the repulsive boundary layer adjacent to the wall. Consequently the solid attracts the gas molecules which counter exert an increasing traction force on the wall as the number of molecules (bulk gas pressure) increases. As the molecules fill completely this zone, the coupled system reaches the most attractive thermodynamic state at point B in Figure 3. On the other hand, with further increase in pressure from the critical point B, the gas gradually moves towards the repulsive zone, with molecules partitioned between the two zones. Therefore the value of Π decreases in magnitude, the traction exerted by the gas molecules on the wall also diminishes. Consequently, the path B$\rightarrow$C is intrinsically linked to matrix swelling.

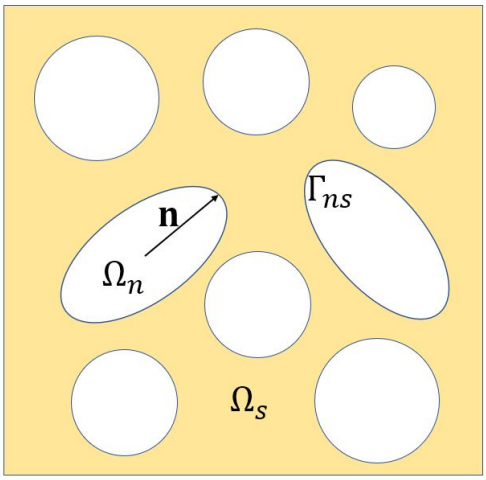

Figure 2: Illustration of the sub-domains in the coal matrix

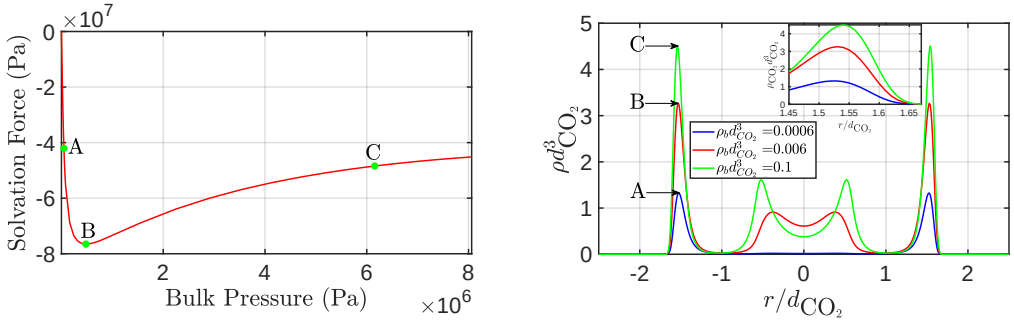

(a) (b)

Figure 3: (a) Solvation force versus CO_2 bulk pressure in a spherical pore of radius $R = 2.5\, d_{CO_2}$. (b) Gas density profiles corresponding to three points for low (A), transition (B) and high (C) bulk pressures [16].

2.2 Non-linear elastic stress in the cleats

In addition to the aforementioned response of the solvation force, one also needs to postulate a constitutive law for the contact stress at the coarser scale. As stated previously, in contrast to earlier work [15], we proceed within a more realistic experimentally-based framework proposed by Barton-Bandis [19, 22, 29, 21]. In this approach, the contact stress is represented in terms of perturbations in the mechanical aperture, characterized by the mean point-wise distance between opposite faces

denoted + and − (see Figure 4). The joint closure due to compression, denoting herein in terms of a

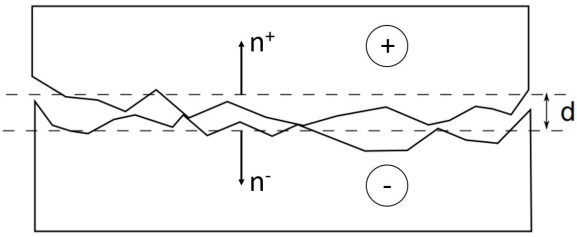

Figure 4: Illustration of the mechanical interaction between opposite joint surfaces.

displacement jump, is defined as the difference between the maximum aperture V_m, measured at the traction-free state, and the crack opening d associated to a loaded state. We have

$$[\![u_n]\!] = d - V_m \tag{3}$$

where $[\![u_n]\!] := \mathbf{u}^+ \cdot \mathbf{n}^+ + \mathbf{u}^- \cdot \mathbf{n}^- = (\mathbf{u}^+ - \mathbf{u}^-) \cdot \mathbf{n}^+$ with $\mathbf{u}^\pm$ and $\mathbf{n}^\pm$ the displacements and the normal vectors on each edge of the cleat (see Figure 4) From the above relation, the bounds $d = V_m$ and $d = 0$, corresponding to $[\![u_n]\!] = 0$ and $[\![u_n]\!] = -V_m$, naturally appear inherent to the cases of totally open (unloaded) and closed joints respectively. Thus, following Barton and Bandis [19], the constitutive relation between joint closure and contact stress is ruled by the hyperbolic equations

$$[\![u_n]\!] = \frac{\bar{\sigma}_n^{\mathrm{BB}} V_m}{K_{ni} V_m - \bar{\sigma}_n^{\mathrm{BB}}} \tag{4}$$

$$\bar{\sigma}_n^{\mathrm{BB}} = \frac{K_{ni} V_m [\![u_n]\!]}{V_m + [\![u_n]\!]} \tag{5}$$

with $\bar{\sigma}_n^{\mathrm{BB}}$ the contact stress and $K_{n,i}$ the initial normal stiffness. Hence, in incremental form we have

$$\mathrm{d}\bar{\sigma}_n^{\mathrm{BB}} = K_n \mathrm{d}[\![u_n]\!] \quad \text{with} \quad K_n := \frac{K_{ni} V_m^2}{(V_m + [\![u_n]\!])^2} \tag{6}$$

the normal stiffness of the joint. Figure 5 shows a typical profile associated with the Barton-Bandis law. One can easily observe a tremendous increase in stiffness K_n as $[\![u_n]\!] \to -V_m$.

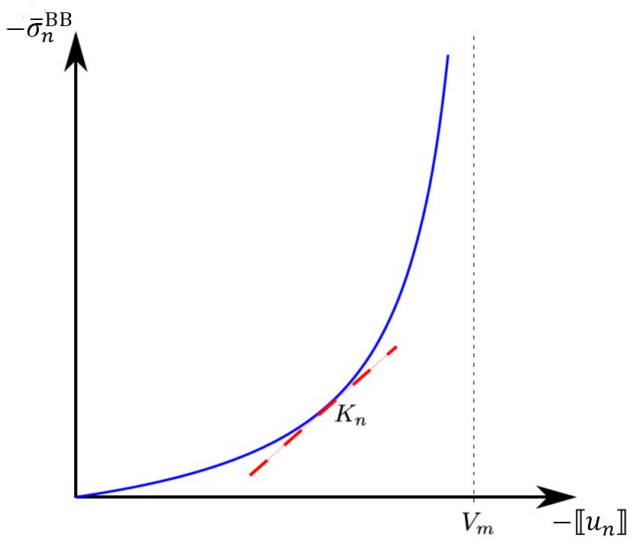

Figure 5: Typical curve associated with the Barton-Bandis constitutive law.

In addition to the normal stress, the shear component admits complex behavior mainly characterized by a peak value and subsequent softening behavior [19, 31]. In particular, in the range of small tangential displacement jump $[[\mathbf{u}_\tau]]$ (lower than 30% of the peak value), the elastic behavior behaves in a nearly linear fashion solely induced by friction mobilization. For simplicity, in our subsequent developments we restrict our analysis to the range of linear dependence of shear stress on tangential displacement ruled by a constant proportionality coefficient $0 < \mu_c \leq 1$ which dictates the ratio between tangential and normal stiffness. Thus, denoting $K_{\tau i}$ the initial shear stiffness we have

$$\frac{K_\tau}{K_{\tau i}} = \frac{K_n}{K_{ni}}, \qquad \text{with} \quad \mu_c := \frac{K_{\tau i}}{K_{ni}} = \frac{K_\tau}{K_n} \tag{7}$$

Finally, denoting $\boldsymbol{\sigma}^+$ and $\boldsymbol{\sigma}^-$ the stresses on the two sides + and − of the fracture, the traction

vector $\boldsymbol{t}_f$ is given by the projection

$$\boldsymbol{t}_f = \boldsymbol{\sigma}^+ \cdot \mathbf{n}^+ = \boldsymbol{\sigma}^- \cdot \mathbf{n}^+ \equiv \boldsymbol{\sigma} \cdot \mathbf{n}^+ \tag{8}$$

whose increment can be represented as

$$\begin{aligned} \mathrm{d}\boldsymbol{\sigma}^+ \cdot \mathbf{n}^+ &= \mathrm{d}\boldsymbol{\sigma}^- \cdot \mathbf{n}^+ \equiv \mathrm{d}\boldsymbol{\sigma} \cdot \mathbf{n}^+ \\ \mathrm{d}\boldsymbol{\sigma} \cdot \mathbf{n}^+ &= K_n [\![\mathrm{d}\mathbf{u}_n]\!] + K_\tau [\![\mathrm{d}\mathbf{u}_\tau]\!] \\ \text{with} \quad [\![\mathrm{d}\mathbf{u}_n]\!] &= (\mathrm{d}\mathbf{u}^+ \cdot \mathbf{n}^+ + \mathrm{d}\mathbf{u}^- \cdot \mathbf{n}^-)\mathbf{n}^+ = [(\mathrm{d}\mathbf{u}^+ - \mathrm{d}\mathbf{u}^-) \cdot \mathbf{n}^+]\mathbf{n}^+ \\ \text{and} \quad [\![\mathrm{d}\mathbf{u}_\tau]\!] &= \mathrm{d}\mathbf{u}^+ - \mathrm{d}\mathbf{u}^- - [\![\mathrm{d}\mathbf{u}_n]\!] \end{aligned} \tag{9}$$

3 Reiterated Homogenization

Hereafter we pursue the upscaling of the nanoscopic description to the microscale aiming at constructing incremental constitutive law for the effective stress and Lagrangian porosity in the coal matrix. Subsequently the microscopic model is homogenized in a reiterated fashion with the cleat system considering the normal traction on the cleat surface ruled by the BB law.

3.1 Nanoscopic Model

By invoking the previous nanoscopic description, our fine scale scenario is characterized by a coal matrix composed of a nanopore system occupied by a mixture of adsorbed gases. The locations associated with the pore space are denoted by the sub-domain Ω_n whereas the complementary solid phase occupies the volume Ω_s. The interface between them is denoted by Γ_{ns}. Under the absence of

gravitational forces, mechanical equilibrium reads as

$$\begin{cases} \boldsymbol{\nabla} \cdot \boldsymbol{\sigma}_n = 0 & \text{in } \Omega_n \\ \boldsymbol{\nabla} \cdot \boldsymbol{\sigma}_s = 0 & \text{in } \Omega_s \end{cases} \tag{10}$$

supplemented by the aforementioned interface conditions

$$\boldsymbol{\sigma}_n \cdot \mathbf{n} = \boldsymbol{\sigma}_s \cdot \mathbf{n} = -(\boldsymbol{\Pi} + p_m \, \mathbf{n}), \quad \text{on} \quad \Gamma_{ns} \tag{11}$$

In addition, the stress tensor in the solid phase is given by

$$\boldsymbol{\sigma}_s = \mathbf{c}_s : \boldsymbol{\mathcal{E}}(\mathbf{u}) \qquad \text{in } \Omega_s \tag{12}$$

where $\mathbf{c}_s$ is the elastic modulus of the solid phase, $\mathbf{u}$ the displacement and $\boldsymbol{\mathcal{E}}(\mathbf{u}) = (\boldsymbol{\nabla}\mathbf{u} + (\boldsymbol{\nabla}\mathbf{u})^{\mathrm{T}})/2$ the linearized deformation.

3.2 Two-scale homogenization

After establishing the nanoscopic model, we proceed within a formal homogenization procedure in order to construct the poromechanics of the coal matrix. Thus, adopting the usual nomenclature, assign a periodic structure to the overall nanoscopic domain $\Omega_n \cup \Omega_s$ which can be reconstructed by replication of a representative unit cell $Z = Z_s \cup Z_n$ along with the solid-fluid interface ∂Z_{ns}. Denoting ℓ_z and L_y the respective characteristic length-scales of the cell and the homogenized matrix, introduce the small perturbation parameter $\varepsilon = \ell_z / L_y$ along with the slow and fast coordinates $\boldsymbol{y}$ and $\boldsymbol{z} = \boldsymbol{y}/\varepsilon$. We postulate the ansatz

$$f^{\varepsilon}(\boldsymbol{y}, \boldsymbol{z}) = \sum_{k=0}^{\infty} \varepsilon^k f^{(k)}(\boldsymbol{y}, \boldsymbol{z}) \tag{13}$$

Under the macroscopic point of view, the spatial operators are given by

$$\boldsymbol{\nabla} f^{\varepsilon}(\boldsymbol{y},\boldsymbol{z}) = \boldsymbol{\nabla}_y f^{\varepsilon}(\boldsymbol{y},\boldsymbol{z}) + \frac{1}{\varepsilon}\boldsymbol{\nabla}_z f^{\varepsilon}(\boldsymbol{y},\boldsymbol{z}) \tag{14}$$

We now proceed by collecting the terms in the different powers of ε. For the solid phase, we have

$$\left\{\begin{array}{ll} \boldsymbol{\nabla}_z \cdot \left[\mathbf{c}_s : \boldsymbol{\mathcal{E}}_z(\mathbf{u}^{(0)})\right] = 0 & \\ \boldsymbol{\nabla}_z \cdot \boldsymbol{\sigma}_s^{(0)} = 0 & \text{in } Z_s \\ \boldsymbol{\nabla}_y \cdot \boldsymbol{\sigma}_s^{(0)} + \boldsymbol{\nabla}_z \cdot \boldsymbol{\sigma}_s^{(1)} = 0 & \\ \boldsymbol{\sigma}_s^{(0)} = \mathbf{c}_s : \left[\boldsymbol{\mathcal{E}}_y(\mathbf{u}^{(0)}) + \boldsymbol{\mathcal{E}}_z(\mathbf{u}^{(1)})\right] & \end{array}\right. \tag{15}$$

and for the gas phase

$$\left\{\begin{array}{ll} \boldsymbol{\nabla}_z \cdot \boldsymbol{\sigma}_n^{(0)} = 0 & \text{in } Z_n \\ \boldsymbol{\nabla}_y \cdot \boldsymbol{\sigma}_n^{(0)} + \boldsymbol{\nabla}_z \cdot \boldsymbol{\sigma}_n^{(1)} = 0 & \end{array}\right. \tag{16}$$

supplemented by the interface conditions

$$\left\{\begin{array}{l} \boldsymbol{\sigma}_n^{(0)} \cdot \mathbf{n} = \boldsymbol{\sigma}_s^{(0)} \cdot \mathbf{n} = -(p_m^{(0)}\mathbf{n} + \boldsymbol{\Pi}^{(0)}) \quad \text{on } \partial Z_{ns} \\ \boldsymbol{\sigma}_n^{(1)} \cdot \mathbf{n} = \boldsymbol{\sigma}_s^{(1)} \cdot \mathbf{n} \end{array}\right. \tag{17}$$

From (15), we have the local rigid motion $\mathbf{u}^{(0)}(\boldsymbol{y},\boldsymbol{z}) = \mathbf{u}^{(0)}(\boldsymbol{y})$. In addition, the fluctuations satisfy the local problem

$$\left\{\begin{array}{lcll} \boldsymbol{\nabla}_z \cdot \left(\mathbf{c}_s : \boldsymbol{\mathcal{E}}_z(\mathbf{u}^{(1)})\right) & = & 0 & \text{in } Z_s \\ \mathbf{c}_s : \left[\boldsymbol{\mathcal{E}}_y(\mathbf{u}^{(0)}) + \boldsymbol{\mathcal{E}}_z(\mathbf{u}^{(1)})\right] \cdot \mathbf{n} & = & -(p_m^{(0)}\mathbf{n} + \boldsymbol{\Pi}^{(0)}) & \text{on } \partial Z_{ns} \end{array}\right. \tag{18}$$

Hence, by invoking linearity, postulate the decomposition of the displacement at order $\mathcal{O}(\varepsilon)$, $\mathbf{u}^{(1)} =$

$\mathbf{u}_e^{(1)} + p_m^{(0)}\boldsymbol{\eta} + \mathbf{u}_\pi^{(1)}$ with the right hand side satisfying the local problems

$$\left\{\begin{array}{rcll} \boldsymbol{\nabla}_z \cdot \left(\mathbf{c}_s : \boldsymbol{\mathcal{E}}_z(\mathbf{u}_e^{(1)})\right) & = & 0 & \text{in } Z_s \\ \mathbf{c}_s : \left[\boldsymbol{\mathcal{E}}_y(\mathbf{u}^{(0)}) + \boldsymbol{\mathcal{E}}_z(\mathbf{u}_e^{(1)})\right] \cdot \mathbf{n} & = & 0 & \text{on } \partial Z_{ns} \end{array}\right. \tag{19}$$

along with

$$\left\{\begin{array}{rcll} \boldsymbol{\nabla}_z \cdot (\mathbf{c}_s : \boldsymbol{\mathcal{E}}_z(\boldsymbol{\eta})) & = & 0 & \text{in } Z_s \\ (\mathbf{c}_s : \boldsymbol{\mathcal{E}}_z(\boldsymbol{\eta}) + \mathbf{I}) \cdot \mathbf{n} & = & 0 & \text{on } \partial Z_{ns} \end{array}\right. \tag{20}$$

and

$$\left\{\begin{array}{rcll} \boldsymbol{\nabla}_z \cdot \left(\mathbf{c}_s : \boldsymbol{\mathcal{E}}_z(\mathbf{u}_\pi^{(1)})\right) & = & 0 & \text{in } Z_s \\ \mathbf{c}_s : \boldsymbol{\mathcal{E}}_z(\mathbf{u}_\pi^{(1)}) \cdot \mathbf{n} & = & -\boldsymbol{\Pi}^{(0)} & \text{on } \partial Z_{ns} \end{array}\right. \tag{21}$$

It should be noted that non-slit and non-spherical pore geometries imply in a non-uniform solvation force profile which inherits the local dependency $\boldsymbol{\Pi}^{(0)} = \boldsymbol{\Pi}^{(0)}(z)$. Consequently, from (21), the component $\mathbf{u}_\pi^{(1)}$ does not admit a straightforward decomposition. Conversely, from classical linear elasticity we have

$$\mathbf{u}_e^{(1)} = \boldsymbol{\xi}(z) : \boldsymbol{\mathcal{E}}_y(\mathbf{u}^{(0)}(\boldsymbol{y})) \tag{22}$$

where the third order tensor $\boldsymbol{\xi}(z)$ satisfies the closure problem

$$\left\{\begin{array}{rcll} \boldsymbol{\nabla}_z \cdot (\mathbf{c}_s : \boldsymbol{\mathcal{E}}_z(\boldsymbol{\xi})) & = & 0 & \text{in } Z_s \\ \mathbf{n} \cdot \mathbf{c}_s : [\mathbb{I} + \boldsymbol{\mathcal{E}}_z(\boldsymbol{\xi})] & = & 0 & \text{on } \partial Z_{ns} \end{array}\right. \tag{23}$$

with $\mathbb{I}$ the fourth-order identity tensor, $\mathbb{I}_{ijkl} := \left(\delta_{ik}\delta_{jl} + \delta_{il}\delta_{jk}\right)/2$ and δ_{ij} the Kronecker delta symbol.

Given the local closure problems for the fluctuations we now pursue the derivation of the upscaled equations. To this end, the total stress tensor for the matrix is defined as

$$\boldsymbol{\sigma}_m^{(0)} = \langle \boldsymbol{\sigma}_n^{(0)} \rangle + \langle \boldsymbol{\sigma}_s^{(0)} \rangle \tag{24}$$

with $\langle . \rangle$ designating the average operator over the unit cell. A straightforward calculation from the equilibrium condition at $O(\varepsilon^0)$ shows $\boldsymbol{\nabla}_y \cdot \boldsymbol{\sigma}_m^{(0)} = 0$. Hence, introducing the effective modulus of the matrix

$$\mathbf{C}_m := \langle \mathbf{c}_s : (\mathbb{I} + \boldsymbol{\mathcal{E}}_z(\boldsymbol{\xi})) \rangle \tag{25}$$

by averaging (15) and using the above-mentioned decompositions we infer

$$\begin{aligned} \langle \boldsymbol{\sigma}_s^{(0)} \rangle &= \langle \mathbf{c}_s : (\mathbb{I} + \boldsymbol{\mathcal{E}}_z(\boldsymbol{\xi})) \rangle : \boldsymbol{\mathcal{E}}_y(\mathbf{u}^{(0)}) + \langle \mathbf{c}_s : \boldsymbol{\mathcal{E}}_z(\boldsymbol{\eta}) \rangle p_m^{(0)} + \langle \mathbf{c}_s : \boldsymbol{\mathcal{E}}_z(\mathbf{u}_\pi^{(1)}) \rangle \\ &= \mathbf{C}_m : \boldsymbol{\mathcal{E}}_y(\mathbf{u}^{(0)}) + \langle \mathbf{c}_s : \boldsymbol{\mathcal{E}}_z(\boldsymbol{\eta}) \rangle p_m^{(0)} + \langle \mathbf{c}_s : \boldsymbol{\mathcal{E}}_z(\mathbf{u}_\pi^{(1)}) \rangle \end{aligned} \tag{26}$$

It remains to compute the component $\langle \boldsymbol{\sigma}_n^{(0)} \rangle$ induced by the solvation force. For the sake of simplicity, the problem here is limited to the case of closed-pore system. By exploring the local equilibrium $\boldsymbol{\nabla}_z \cdot \boldsymbol{\sigma}_n^{(0)} = 0$ and the symmetry of the Cauchy stress tensor, the third order tensor $\boldsymbol{\sigma}_n^{(0)} \otimes \boldsymbol{z}$ satisfies the relation

$$\boldsymbol{\nabla}_z \cdot (\boldsymbol{\sigma}_n^{(0)} \otimes \boldsymbol{z}) = \boldsymbol{\sigma}_n^{(0)} \tag{27}$$

By using the divergence theorem along with the interface condition (17) we obtain

$$\begin{aligned}\langle \boldsymbol{\sigma}_n^{(0)} \rangle &= \langle \boldsymbol{\nabla}_z \cdot (\boldsymbol{\sigma}_n^{(0)} \otimes \boldsymbol{z}) \rangle = \frac{1}{|Z|} \int_{\partial Z_{ns}} \mathbf{n} \cdot \left(\boldsymbol{\sigma}_n^{(0)} \otimes \boldsymbol{z} \right) \mathrm{d}S \\ &= \frac{1}{|Z|} \int_{\partial Z_{ns}} \left(\boldsymbol{\sigma}_n^{(0)} \cdot \mathbf{n} \right) \otimes \boldsymbol{z} \, \mathrm{d}S = -\frac{1}{|Z|} \int_{\partial Z_{ns}} (p_m^{(0)} \mathbf{n} + \boldsymbol{\Pi}^{(0)}) \otimes \boldsymbol{z} \, \mathrm{d}S \\ &= -\phi_m p_m^{(0)} \mathbf{I} - \frac{1}{|Z|} \int_{\partial Z_{ns}} \boldsymbol{\Pi}^{(0)} \otimes \boldsymbol{z} \, \mathrm{d}S \end{aligned} \tag{28}$$

with $|Z|$ the local cell volume. Finally, by collecting our previous results, the total stress tensor in the matrix admits the generalized effective stress decomposition

$$\boldsymbol{\sigma}_m^{(0)} = \mathbf{C}_m : \boldsymbol{\mathcal{E}}_y(\mathbf{u}^{(0)}) - \boldsymbol{\alpha}_m p_m^{(0)} + \langle \mathbf{c}_s : \boldsymbol{\mathcal{E}}_z(\mathbf{u}_\pi^{(1)}) \rangle - \frac{1}{|Z|} \int_{\partial Z_{ns}} \boldsymbol{\Pi}^{(0)} \otimes \boldsymbol{z} \, \mathrm{d}S \tag{29}$$

Hence, using the classical relation $\langle \mathbf{c}_s : \boldsymbol{\mathcal{E}}_z(\boldsymbol{\eta}) \rangle = \langle \boldsymbol{\nabla}_z \cdot \boldsymbol{\xi} \rangle$ along with the definition of the Biot-Willis tensor [32]

$$\boldsymbol{\alpha}_m = \phi_m \mathbf{I} - \langle \mathbf{c}_s : \boldsymbol{\mathcal{E}}_z(\boldsymbol{\eta}) \rangle = \phi_m \mathbf{I} - \langle \boldsymbol{\nabla}_z \cdot \boldsymbol{\xi} \rangle \tag{30}$$

and defining the swelling tensor as

$$\boldsymbol{F}_S = \langle \mathbf{c}_s : \boldsymbol{\mathcal{E}}_z(\mathbf{u}_\pi^{(1)}) \rangle - \frac{1}{|Z|} \int_{\partial Z_{ns}} \boldsymbol{\Pi}^{(0)} \otimes \boldsymbol{z} \mathrm{d}S \tag{31}$$

the total stress tensor admits the representation

$$\boldsymbol{\sigma}_m^{(0)} = \mathbf{C}_m : \boldsymbol{\mathcal{E}}_y(\mathbf{u}^{(0)}) - \boldsymbol{\alpha}_m p_m^{(0)} + \boldsymbol{F}_S \tag{32}$$

which consists of the classical effective stress principle with the additional component involving the solvation force.

We are now ready to state the two-scale poromechanical model for the coal matrix. Let Ω_m be the domain occupied by the matrix. Given the usual local representations of the pair of poroelastic

coefficients $\{\boldsymbol{\alpha}_m, \mathbf{C}_m\}$ along with the nanoscopic representation for the solvation force and the pore pressure profile in the reference bulk gas in the matrix $p_m^{(0)} = p_m^{(0)}(\boldsymbol{y})$, we seek the pair $\{\boldsymbol{\sigma}_m^{(0)}, \mathbf{u}^{(0)}\}$ satisfying

$$\left\{\begin{array}{rcll} \boldsymbol{\nabla}_y \cdot \boldsymbol{\sigma}_m^{(0)} & = & 0 & \text{in } \Omega_m \\ \boldsymbol{\sigma}_m^{(0)} & = & \mathbf{C}_m : \boldsymbol{\mathcal{E}}_y(\mathbf{u}^{(0)}) - \boldsymbol{\alpha}_m p_m^{(0)} + \boldsymbol{F}_S & \end{array}\right. \tag{33}$$

By comparing with the effective stress principle of traditional poroelasticity, the novelty here is the inclusion of the solvation force component, which, for a given pore geometry, can be accurately computed from the nanoscopic representation.

3.3 Incremental formulation

The appearance of the solvation force induces a strong non-linearity as $\boldsymbol{F}_s$ depends in a non-linear fashion on the partial pressure of each gas in a mixture of N components $p_{m,i}$, $(i = 1, ..., N)$ along with the Lagrangian porosity of the matrix ϕ_m. Whence, following the traditional framework of non-linear solid mechanics, we proceed by rephrasing the modified effective stress principle in incremental form from a prescribed reference state.

3.3.1 General setting

Without loss of generality, consider the swelling tensor $\boldsymbol{F}_s$ depending only on the pressures $p_{m,i}$ and the porosity ϕ_m. This yields

$$\mathrm{d}\boldsymbol{\sigma}_m^{(0)} = \mathbf{C}_m : \boldsymbol{\mathcal{E}}\left(\mathrm{d}\mathbf{u}^{(0)}\right) - \boldsymbol{\alpha}_m \mathrm{d}p_m^{(0)} + \sum_{i=1}^{N} \boldsymbol{\gamma}_i \, \mathrm{d}p_{m,i}^{(0)} + \boldsymbol{\nu} \, \mathrm{d}\phi_m \tag{34}$$

with

$$\boldsymbol{\gamma}_i := \frac{\partial \boldsymbol{F}_S}{\partial p_{m,i}^{(0)}} \quad \text{and} \quad \boldsymbol{\nu} := \frac{\partial \boldsymbol{F}_S}{\partial \phi_m} \tag{35}$$

Given the incremental form of the total stress in the matrix, to complete the two-scale model, it remains to establish the constitutive law for the Lagrangian porosity relative to the reference state. To this end, one needs to characterize an extension of the displacement of the solid phase over the fluid phase. This can be accomplished by simply filling the voids with a fictitious poroelastic system with negligible stiffness which plays none role in the equilibrium. This yields the extension

$$\begin{cases} \mathbf{u} & := & \mathbf{u}_s & \text{in } Z_s \\ \mathbf{u} & := & \mathbf{u}_n & \text{in } Z_n \end{cases} \tag{36}$$

together with the continuity condition at the interface $\mathbf{u}_s \cdot \mathbf{n}_{ns} = \mathbf{u}_n \cdot \mathbf{n}_{ns}$.

By definition, the incremental Lagrangian porosity is given by

$$\mathrm{d}\phi_m = \frac{\mathrm{d}|Z_n|}{|Z|} = \frac{1}{|Z|}\int_{\partial Z_n} \mathrm{d}\mathbf{u}_n \cdot \mathbf{n}_n \mathrm{d}S \tag{37}$$

Considering the closed-pore domain Z_n of external surface $\partial Z_n = \partial Z_{ns}$ inside the unit cell $Z = Z_n \cup Z_s$, we have

$$\begin{aligned} \mathrm{d}\phi_m &= \frac{1}{|Z|}\int_{\partial Z_{ns}} \mathrm{d}\mathbf{u}_n \cdot \mathbf{n}_{ns}\mathrm{d}S = \frac{1}{|Z|}\int_{Z_n} \boldsymbol{\nabla} \cdot \mathrm{d}\mathbf{u}_n \mathrm{d}V \\ &= \frac{1}{|Z|}\int_{Z} \boldsymbol{\nabla} \cdot \mathrm{d}\mathbf{u}\, \mathrm{d}V - \frac{1}{|Z|}\int_{Z_s} \boldsymbol{\nabla} \cdot \mathrm{d}\mathbf{u}_s\, \mathrm{d}V \\ &= \langle \boldsymbol{\nabla} \cdot \mathrm{d}\mathbf{u} \rangle - (1-\phi_m)\langle \boldsymbol{\nabla} \cdot \mathrm{d}\mathbf{u}_s \rangle^s \end{aligned} \tag{38}$$

where $\langle . \rangle^s = \langle\ \rangle/(1-\phi_m)$ is the intrinsic volume average over the solid phase. Thus, after invoking periodicity together with the rigid motion at $O\ (1)$, the first term in the r.h.s. can be rewritten as

$$\langle \boldsymbol{\nabla} \cdot \mathrm{d}\mathbf{u} \rangle = \langle \boldsymbol{\nabla}_y \cdot \mathrm{d}\mathbf{u}^{(0)} + \boldsymbol{\nabla}_z \cdot \mathrm{d}\mathbf{u}^{(1)} \rangle = \boldsymbol{\nabla}_y \cdot \mathrm{d}\mathbf{u}^{(0)} + \frac{1}{|Z|}\int_{\partial Z} \mathrm{d}\mathbf{u}^{(1)} \cdot \mathbf{n}_e \mathrm{d}S = \boldsymbol{\nabla}_y \cdot \mathrm{d}\mathbf{u}^{(0)} = \boldsymbol{\nabla}_y \cdot \mathrm{d}\mathbf{u}_s^{(0)} \tag{39}$$

where the integral term vanishes invoking periodicity. The intrinsic average of the divergence of the

solid displacement can be written

$$\langle \boldsymbol{\nabla} \cdot \mathrm{d}\mathbf{u}_s \rangle^s = \boldsymbol{\nabla}_y \cdot \mathrm{d}\mathbf{u}_s^{(0)} + \langle \boldsymbol{\nabla}_z \cdot \mathrm{d}\mathbf{u}_s^{(1)} \rangle^s \tag{40}$$

221 Inserting the above results in (38) we obtain

$$\mathrm{d}\phi_m = \phi_m \boldsymbol{\nabla}_y \cdot \mathrm{d}\mathbf{u}^{(0)} - \left\langle \boldsymbol{\nabla}_z \cdot \mathrm{d}\mathbf{u}^{(1)} \right\rangle \tag{41}$$

By invoking the aforementioned decomposition for the displacement fluctuation

$$\mathrm{d}\mathbf{u}^{(1)} = \boldsymbol{\xi} : \boldsymbol{\mathcal{E}}_y \left(\mathrm{d}\mathbf{u}^{(0)} \right) + \mathrm{d}p_m^{(0)} \boldsymbol{\eta} + \mathrm{d}\mathbf{u}_\pi^{(1)} \tag{42}$$

we infer

$$\left\langle \boldsymbol{\nabla}_z \cdot \mathrm{d}\mathbf{u}^{(1)} \right\rangle = \langle \boldsymbol{\nabla}_z \cdot \boldsymbol{\xi} \rangle : \boldsymbol{\mathcal{E}}_y \left(\mathrm{d}\mathbf{u}^{(0)} \right) + \mathrm{d}p_m^{(0)} \langle \boldsymbol{\nabla}_z \cdot \boldsymbol{\eta} \rangle + \left\langle \boldsymbol{\nabla}_z \cdot \mathrm{d}\mathbf{u}_\pi^{(1)} \right\rangle \tag{43}$$

222 Recalling the representation for the Biot-Willis parameter (30)

$$\langle \boldsymbol{\nabla}_z \cdot \boldsymbol{\xi} \rangle = \phi_m \mathbf{I} - \boldsymbol{\alpha}_m \tag{44}$$

223 and combining relations (41) and (43) lead to

$$\mathrm{d}\phi_m = \boldsymbol{\alpha}_m : \boldsymbol{\mathcal{E}}_y \left(\mathrm{d}\mathbf{u}^{(0)} \right) - \mathrm{d}p_m^{(0)} \langle \boldsymbol{\nabla}_z \cdot \boldsymbol{\eta} \rangle - \left\langle \boldsymbol{\nabla}_z \cdot \mathrm{d}\mathbf{u}_\pi^{(1)} \right\rangle \tag{45}$$

Introducing the matrix compressibility with respect to each partial gas pressure, including mechanical and solvation components in the form

$$\beta_i = -\frac{\partial}{\partial p_{m,i}^{(0)}} \left(\left\langle \boldsymbol{\nabla}_z \cdot \mathbf{u}_\pi^{(1)} \right\rangle \right) - \langle \boldsymbol{\nabla}_z \cdot \boldsymbol{\eta} \rangle \tag{46}$$

and considering $p_m = \sum_i p_{m,i}$, we obtain

$$\mathrm{d}\phi_m = \boldsymbol{\alpha}_m : \boldsymbol{\mathcal{E}}_y \left(\mathrm{d}\mathbf{u}^{(0)}\right) + \sum_{i=1}^{N} \beta_i \, \mathrm{d}p_{m,i}^{(0)} \tag{47}$$

Hence, combination with (34) gives the incremental form of the effective stress principle

$$\mathrm{d}\boldsymbol{\sigma}_m^{(0)} = \mathbf{C}_m^* : \boldsymbol{\mathcal{E}} \left(\mathrm{d}\mathbf{u}^{(0)}\right) + \sum_{i=1}^{N} (\boldsymbol{\gamma}_i + \boldsymbol{\nu}\,\beta_i - \boldsymbol{\alpha}_m) \, \mathrm{d}p_{m,i}^{(0)} \tag{48}$$

$$\text{with} \quad \mathbf{C}_m^* = \mathbf{C}_m + \boldsymbol{\nu} \otimes \boldsymbol{\alpha}_m \tag{49}$$

which leads to a new tangent modulus for the matrix including the component of the solvation force associated with changes in matrix porosity. Moreover, the modified Biot-Willis parameter which also incorporates the effects of the solvation force reads as

$$\boldsymbol{\alpha}_{m,i}^* := \boldsymbol{\alpha}_m - \boldsymbol{\gamma}_i - \boldsymbol{\nu}\,\beta_i \tag{50}$$

Thus, in terms of an effective stress, the incremental decomposition (48) can be rewritten as

$$\mathrm{d}\boldsymbol{\sigma}_m^{(0)} = \mathbf{C}_m^* : \boldsymbol{\mathcal{E}} \left(\mathrm{d}\mathbf{u}^{(0)}\right) - \sum_{i=1}^{N} \boldsymbol{\alpha}_{m,i}^* \mathrm{d}p_{m,i}^{(0)} \tag{51}$$

It is noteworthy that, unlike $\boldsymbol{\alpha}_m$, the modified parameter $\boldsymbol{\alpha}_{m,i}^*$ is not a single property of the matrix but also carries the index associated with each gas in the mixture.

3.3.2 Isotropic configuration of spherical nanopores

For the sake of simplicity and without loss of generality, hereafter we consider the scenario of spherical pores. In this configuration, isotropy implies in reduction of both $\boldsymbol{\Pi}^{(0)}$ to a scalar quantity acting in the normal direction to the surface $\boldsymbol{\Pi}^{(0)} = \Pi^{(0)}\mathbf{n}$, and the tensorial swelling stress to a spherical scalar

quantity $\boldsymbol{F}_S = F_S\,\mathbf{I}$. Thus, denoting R the radius of the sphere and $\mathbf{n}$ the unit outward normal, by invoking (28) along with the relation

$$\int_S \mathbf{n}\otimes\mathbf{n}\,\mathrm{d}S = \frac{4}{3}\pi R^2\,\mathbf{I} \tag{52}$$

we infer

$$\begin{aligned}\langle\boldsymbol{\sigma}_n^{(0)}\rangle &= -\phi_m p_m^{(0)} - \frac{1}{|Z|}\int_{\partial Z_{ns}} \boldsymbol{\Pi}^{(0)}\otimes z\,\mathrm{d}S = -\phi_m p_m^{(0)} - \Pi^{(0)}\frac{1}{|Z|}\int_{\partial Z_{ns}}\mathbf{n}\otimes(R\,\mathbf{n})\,\mathrm{d}S\\ &= -\phi_m(p_m^{(0)}+\Pi^{(0)})\mathbf{I}\end{aligned} \tag{53}$$

Further, since Π is constant for spherical pores, by invoking definition (20), the closure problem (21) for $\mathbf{u}_\pi^{(1)}$ admits the decomposition

$$\mathbf{u}_\pi^{(1)} = \Pi^{(0)}\boldsymbol{\eta} \tag{54}$$

The above result can be explored to obtain the reduced representation for the first term of the r.h.s. of (31) in the form

$$\langle\mathbf{c}_s : \boldsymbol{\mathcal{E}}_z(\mathbf{u}_\pi^{(1)})\rangle = \langle\mathbf{c}_s : \boldsymbol{\mathcal{E}}_z(\boldsymbol{\eta})\rangle\Pi^{(0)} \tag{55}$$

Combining with (30), the swelling tensor (31) becomes

$$\boldsymbol{F}_s = (\langle\mathbf{c}_s : \boldsymbol{\mathcal{E}}_z(\boldsymbol{\eta})\rangle - \phi_m\mathbf{I})\,\Pi^{(0)} = -\boldsymbol{\alpha}_m\Pi^{(0)} \tag{56}$$

Using the above representation in the modified effective stress principle (32) gives

$$\begin{aligned}\boldsymbol{\sigma}_m^{(0)} &= \mathbf{C}_m : \boldsymbol{\mathcal{E}}_y(\mathbf{u}^{(0)}) - (p_m^{(0)}+\Pi^{(0)})\,(\phi_m\mathbf{I} - \langle\mathbf{c}_s : \boldsymbol{\mathcal{E}}_z(\boldsymbol{\eta})\rangle)\\ &= \mathbf{C}_m : \boldsymbol{\mathcal{E}}_y(\mathbf{u}^{(0)}) - (p_m^{(0)}+\Pi^{(0)})\boldsymbol{\alpha}_m\end{aligned} \tag{57}$$

In addition, under isotropy, the tensorial coefficients of the incremental effective stress principle (48) reduce to scalars (denoted herein without boldface), leading to

$$\mathrm{d}\boldsymbol{\sigma}_m = \mathbf{C}_m^* : \boldsymbol{\mathcal{E}}\,(\mathrm{d}\mathbf{u}) - \sum_{i=1}^{N} \alpha_{m,i}^* \mathrm{d}p_{m,i}\mathbf{I} \tag{58}$$

$$\text{with} \quad \mathbf{C}_m^* = \mathbf{C}_m + \nu\,\alpha_m\,\mathbf{I}\otimes\mathbf{I} \quad \text{and} \quad \alpha_{m,i}^* = \alpha_m - \gamma_i - \nu\,\beta_i \tag{59}$$

Finally, by invoking (45) together with the relation $\langle \boldsymbol{\nabla}_z \cdot \mathbf{u}_\pi^{(1)} \rangle = \Pi^0 \langle \boldsymbol{\nabla}_z \cdot \boldsymbol{\eta} \rangle$, this yields

$$\begin{aligned} \mathrm{d}\phi_m &= \alpha_m \boldsymbol{\nabla}_y \cdot \mathrm{d}\mathbf{u}^{(0)} - \mathrm{d}p_m^{(0)}\,\langle \boldsymbol{\nabla}_z \cdot \boldsymbol{\eta} \rangle - \left\langle \boldsymbol{\nabla}_z \cdot \mathrm{d}\mathbf{u}_\pi^{(1)} \right\rangle \\ &= \alpha_m \boldsymbol{\nabla}_y \cdot \mathrm{d}\mathbf{u}^{(0)} - \sum_{i=1}^{N} \langle \boldsymbol{\nabla}_z \cdot \boldsymbol{\eta} \rangle (\mathrm{d}p_{m,i}^{(0)} + \mathrm{d}\Pi^0) \end{aligned} \tag{60}$$

Hence, by invoking the constitutive dependency $\mathrm{d}\Pi^0 = \mathrm{d}\Pi^0(\mathrm{d}\mathbf{u}^{(0)}, \mathrm{d}p_{m,i}^{(0)})$, the last term in the r.h.s. can be rephrased in the form $\mathrm{d}\Pi^0 = \sum_{i=1}^{N} (\partial\Pi/\partial p_{m,i}) \mathrm{d}p_{m,i}$. By comparing with (47) we have

$$\mathrm{d}\phi_m = \alpha_m \boldsymbol{\nabla}_y \cdot \mathrm{d}\mathbf{u}^{(0)} + \sum_{i=1}^{N} \beta_i\, \mathrm{d}p_{m,i}^{(0)} \tag{61}$$

with β_i given by (46). Further, denoting k_s the bulk modulus of the solid grains [32], under isotropy we have $\langle \boldsymbol{\nabla}_z \cdot \boldsymbol{\eta} \rangle = -\,(\alpha_m - \phi_m)\,/k_s$. Whence, the overall undrained compressibility is given by

$$\beta_i = \left(\frac{\partial \Pi}{\partial p_{m,i}} + 1 \right) \frac{\alpha_m - \phi_m}{k_s} \tag{62}$$

which consists of the traditional poroelastic value supplemented by an additional component involving the response of the solvation force with gas pressure under isochoric conditions.

3.4 Homogenization with the cleat network

We shall henceforth discuss the micro-macro upscaling by incorporating the discrete cleat network in the poromechanical model. To this end, we combine the aforementioned poromechanical description of the matrix with the non-linear elastic response of cleats described by the Barton-Bandis (BB) law. It is worth mentioning the mixed-dimensional nature of the coupled problem, since the cleats are treated as $(n-1)$-manifolds $(n = 2, 3)$ governed by a reduced poromechanics model ruled by the BB law. Thus denoting ℓ_y and L_x the respective characteristic length-scales of the micro and macroscopic descriptions, the perturbation parameter is rephrased as $\varepsilon = \ell_y / L_x$, whereas the slow and fast coordinates are now denoted by $\boldsymbol{x}$ and $\boldsymbol{y} = \boldsymbol{x}/\varepsilon$ respectively. The microscopic periodic cell, designated by Y is occupied by the matrix domain Y_m which is intertwined by interface ∂Y_{mf} associated with the lower dimension cleat network.

3.4.1 Microscopic model

For the sake of completeness and conciseness of notation, the incremental microscopic formulation is revisited herein with subscripts and superscripts omitted for convenience. We then have

$$\begin{cases} \boldsymbol{\nabla} \cdot \mathrm{d}\boldsymbol{\sigma}_m = 0 \\ \mathrm{d}\boldsymbol{\sigma}_m = \mathbf{C}_m^* : \boldsymbol{\mathcal{E}}(\mathrm{d}\mathbf{u}) - \sum_{i=1}^{N} \boldsymbol{\alpha}_{m,i}^* \mathrm{d}p_{m,i} \\ \mathrm{d}\phi_m = \boldsymbol{\alpha}_m : \boldsymbol{\mathcal{E}}_y\,(\mathrm{d}\mathbf{u}) + \sum_{i=1} \beta_i\, \mathrm{d}p_{m,i} \end{cases} \tag{63}$$

We now invoke continuity of normal component of the total matrix stress and the fluid pressure at the matrix/cleat interface. Considering the traction given by the Bandis-Barton law in Section 2.2, denoting $p_{f,i}$, p_f and α_f the partial pressure, total pressure and Biot coefficient of the fracture, the

incremental form of transmission condition reads as

$$\begin{aligned} \mathrm{d}\boldsymbol{\sigma}_m \cdot \mathbf{n}^+ &= K_n [\![\mathrm{d}\mathbf{u}_n]\!] + K_\tau [\![\mathrm{d}\mathbf{u}_\tau]\!] - \alpha_f \, \mathrm{d}p_f \, \mathbf{n}^+ \\ \mathrm{d}p_{m,i} &= \mathrm{d}p_{f,i} \end{aligned} \tag{64}$$

It is noteworthy that the last term in the r.h.s embodies the Biot-Willis coefficient of the cleats α_f. The BB law (64) underlying this parameter may bring an extra dependence on gas pressure. More precisely in D we deduce the relation between α_f and the BB-parameters. A value $\alpha_f = 1$ corresponds to the case where the strain induced by the gas pressure is entirely associated with the cleat/matrix interface.

Further, in order to restrict the effects of the BB law to stress fluctuations within each cell at $O(\varepsilon)$, the first term in r.h.s shall be re-scaled. This yields

$$\mathrm{d}\boldsymbol{\sigma}_m^{(\varepsilon)} \cdot \mathbf{n}^+ = \varepsilon^{-1} \left(K_n [\![\mathrm{d}\mathbf{u}_n^{(\varepsilon)}]\!] + K_\tau [\![\mathrm{d}\mathbf{u}_\tau^{(\varepsilon)}]\!] \right) - \alpha_f \, \mathrm{d}p_f^{(\varepsilon)} \, \mathbf{n}^+ \tag{65}$$

3.4.2 Micro-Macro Homogenization

By writing the above results at successive orders of ε gives

$$\begin{cases} O(\varepsilon^{-2}) \;:\; \boldsymbol{\nabla}_y \cdot \left[\mathbf{C}_m^* : \boldsymbol{\mathcal{E}}_y(\mathrm{d}\mathbf{u}^{(0)}) \right] = 0 \\ O(\varepsilon^{-1}) \;:\; \boldsymbol{\nabla}_y \cdot \mathrm{d}\boldsymbol{\sigma}_m^{(0)} = 0 \\ \qquad\qquad \mathrm{d}\boldsymbol{\sigma}_m^{(0)} = \mathbf{C}_m^* : \left[\boldsymbol{\mathcal{E}}_x(\mathrm{d}\mathbf{u}^{(0)}) + \boldsymbol{\mathcal{E}}_y(\mathrm{d}\mathbf{u}^{(1)}) \right] - \sum_{i=1}^N \boldsymbol{\alpha}_{m,i}^* \, \mathrm{d}p_{m,i}^{(0)} \\ O(\varepsilon^0) \;:\; \boldsymbol{\nabla}_x \cdot \mathrm{d}\boldsymbol{\sigma}_m^{(0)} + \boldsymbol{\nabla}_y \cdot \mathrm{d}\boldsymbol{\sigma}_m^{(1)} = 0 \end{cases} \tag{66}$$

along with perturbed boundary conditions at the matrix/cleat interface

$$\left\{\begin{array}{lcll} O(\varepsilon^{-1}) & : & \mathbf{C}_m^* : \boldsymbol{\mathcal{E}}_y(\mathrm{d}\mathbf{u}^{+(0)}) \cdot \mathbf{n}^+ & = \\ & & \mathbf{C}_m^* : \boldsymbol{\mathcal{E}}_y(\mathrm{d}\mathbf{u}^{-(0)}) \cdot \mathbf{n}^+ & = K_n[\![\mathrm{d}\mathbf{u}_n^{(0)}]\!] + K_\tau[\![\mathrm{d}\mathbf{u}_\tau^{(0)}]\!] \\ O(\varepsilon^{0}) & : & \mathbf{C}_m^* : \left[\boldsymbol{\mathcal{E}}_x(\mathrm{d}\mathbf{u}^{+(0)}) + \boldsymbol{\mathcal{E}}_y(\mathrm{d}\mathbf{u}^{+(1)})\right] \cdot \mathbf{n}^+ & = \\ & & \mathbf{C}_m^* : \left[\boldsymbol{\mathcal{E}}_x(\mathrm{d}\mathbf{u}^{-(0)}) + \boldsymbol{\mathcal{E}}_y(\mathrm{d}\mathbf{u}^{-(1)})\right] \cdot \mathbf{n}^+ & = K_n[\![\mathrm{d}\mathbf{u}_n^{(1)}]\!] + K_\tau[\![\mathrm{d}\mathbf{u}_\tau^{(1)}]\!] \\ & & & - \sum_{i=1}^N (\alpha_f \mathbf{I} - \boldsymbol{\alpha}_{m,i}^*)\, \mathrm{d}p_{m,i}^{(0)} \cdot \mathbf{n}^+ \end{array}\right. \tag{67}$$

By invoking (66a) and (67a), our macroscopic slow variables are $\mathrm{d}\mathbf{u}^{(0)}(\boldsymbol{x}, \boldsymbol{y}, t) = \mathrm{d}\mathbf{u}^{(0)}(\boldsymbol{x}, t)$ and $[\![\mathrm{d}\mathbf{u}_n^{(0)}]\!] = [\![\mathrm{d}\mathbf{u}_\tau^{(0)}]\!] = 0$. Such a result induced by the re-scaling in (65) implies that, at $O(\varepsilon^0)$, cleats and matrix behave as a rigid body in each cell and consequently the BB closure affects only the displacement fluctuations. In addition, the closure problem for $\mathbf{u}^{(1)}$ reads as

$$\left\{\begin{array}{lcll} \boldsymbol{\nabla}_y \cdot \left[\mathbf{C}_m^* : \boldsymbol{\mathcal{E}}_y(\mathrm{d}\mathbf{u}^{(1)})\right] & = & \sum_{i=1}^N \boldsymbol{\nabla}_y \cdot \left(\boldsymbol{\alpha}_{m,i}^* \mathrm{d}p_{m,i}^0\right) & \text{in } Y_m \\ \mathbf{C}_m^* : \left[\boldsymbol{\mathcal{E}}_x(\mathrm{d}\mathbf{u}^{(0)}) + \boldsymbol{\mathcal{E}}_y(\mathrm{d}\mathbf{u}^{+(1)})\right] \cdot \mathbf{n}^+ & = & & \\ \mathbf{C}_m^* : \left[\boldsymbol{\mathcal{E}}_x(\mathrm{d}\mathbf{u}^{(0)}) + \boldsymbol{\mathcal{E}}_y(\mathrm{d}\mathbf{u}^{-(1)})\right] \cdot \mathbf{n}^+ & = & K_n[\![\mathrm{d}\mathbf{u}_n^{(1)}]\!] + K_\tau[\![\mathrm{d}\mathbf{u}_\tau^{(1)}]\!] & \\ & & - \sum_{i=1}^N (\alpha_f \mathbf{I} - \boldsymbol{\alpha}_{m,i}^*)\, \mathrm{d}p_{f,i}^{(0)} \cdot \mathbf{n}^+ & \text{on } \partial Y_{mf} \end{array}\right. \tag{68}$$

Since our aim is to focus on the poromechanics, for a prescribed macroscopic gas pressure path in the time-domain $p_{f,i}^{(0)} = p_{f,i}^{(0)}(\boldsymbol{x}, t)$, under local equilibrium condition equilibrium we have $p_{m,i}^{(0)} = p_{f,i}^{(0)} = p_{f,i}^{(0)}(\boldsymbol{x}, t)$. Such a hydraulic communication between the pore pressures precludes the local variability $p_{m,i}^{(0)}(\boldsymbol{y})$ implying that the r.h.s of (68a) vanishes. It should be noted that under unsteady conditions where $p_{m,i}^{(0)} = p_{m,i}^{(0)}(\boldsymbol{x}, \boldsymbol{y}, t)$, an additional source term related to the matrix/cleat pressure difference, which commonly appears in double-porosity-type models shall be added [33, 14].

By adopting a superposition analogous to the two-scale problem, by linearity $\mathrm{d}\mathbf{u}^{(1)}$ can be decomposed in the form $\mathrm{d}\mathbf{u}^{(1)} = \mathrm{d}\mathbf{u}_e^{(1)} + \mathrm{d}\mathbf{u}_\pi^{(1)}$ corresponding to the elastic and solvation components. This

yields

$$\left\{\begin{array}{rcll} \boldsymbol{\nabla}_y \cdot \left[\mathbf{C}^*_m : \boldsymbol{\mathcal{E}}_y(\mathrm{d}\mathbf{u}^{(1)}_e)\right] & = & 0 & \text{in } Y_m \\ \mathbf{C}^*_m : \left[\boldsymbol{\mathcal{E}}_x(\mathrm{d}\mathbf{u}^{(0)}_e) + \boldsymbol{\mathcal{E}}_y(\mathrm{d}\mathbf{u}^{+(1)}_e)\right] \cdot \mathbf{n}^+ & = & \mathbf{C}^*_m : \left[\boldsymbol{\mathcal{E}}_x(\mathrm{d}\mathbf{u}^{(0)}_e) + \boldsymbol{\mathcal{E}}_y(\mathrm{d}\mathbf{u}^{-(1)}_e)\right] \cdot \mathbf{n}^+ & \\ & = & K_n[\![\mathrm{d}\mathbf{u}^{(1)}_{e,n}]\!] + K_\tau[\![\mathrm{d}\mathbf{u}^{(1)}_{e,\tau}]\!] & \text{on } \partial Y_{mf} \end{array}\right. \tag{69}$$

and

$$\left\{\begin{array}{rcll} \boldsymbol{\nabla}_y \cdot \left[\mathbf{C}^*_m : \boldsymbol{\mathcal{E}}_y(\mathrm{d}\mathbf{u}^{(1)}_\pi)\right] & = & 0 & \text{in } Y_m \\ \mathbf{C}^*_m : \left[\boldsymbol{\mathcal{E}}_y(\mathrm{d}\mathbf{u}^{+(1)}_\pi)\right] \cdot \mathbf{n}^+ & = & \mathbf{C}^*_m : \left[\boldsymbol{\mathcal{E}}_y(\mathrm{d}\mathbf{u}^{-(1)}_\pi)\right] \cdot \mathbf{n}^+ & \\ & = & K_n[\![\mathrm{d}\mathbf{u}^{(1)}_{\pi,n}]\!] + K_\tau[\![\mathrm{d}\mathbf{u}^{(1)}_{\pi,\tau}]\!] & \\ & & -\sum_{i=1}^N (\alpha_f \mathbf{I} - \boldsymbol{\alpha}^*_{m,i})\,\mathrm{d}p^{(0)}_{f,i} \cdot \mathbf{n}^+ & \text{on } \partial Y_{mf} \end{array}\right. \tag{70}$$

where $[\![\mathrm{d}\mathbf{u}^{(1)}_{e,n}]\!]$, $[\![\mathrm{d}\mathbf{u}^{(1)}_{e,\tau}]\!]$, $[\![\mathrm{d}\mathbf{u}^{(1)}_{\pi,n}]\!]$ and $[\![\mathrm{d}\mathbf{u}^{(1)}_{\pi,\tau}]\!]$ are the normal/tangential displacement jumps corresponding to the elastic and solvation effects respectively. Likewise, as $\mathrm{d}\mathbf{u}^{(1)}_e$ depends linearly on $\boldsymbol{\mathcal{E}}_x(\mathrm{d}\mathbf{u}^{(0)})$ we infer

$$\mathrm{d}\mathbf{u}^{(1)} = \boldsymbol{\xi} : \boldsymbol{\mathcal{E}}_x(\mathrm{d}\mathbf{u}^{(0)}) + \mathrm{d}\mathbf{u}^{(1)}_\pi \tag{71}$$

Unlike the two-scale counterpart in (23), where the third-order tensor consists of a purely geometrical quantity, here the third-order tensor $\boldsymbol{\xi}$ also incorporates dependence on the non-linear joint BB-stiffness which brings indirect dependence on the partial gas pressures

$$\left\{\begin{array}{rcll} \boldsymbol{\nabla}_y \cdot \left[\mathbf{C}^*_m : \boldsymbol{\mathcal{E}}_y(\boldsymbol{\xi})\right] & = & 0 & \text{in } Y_m \\ \mathbf{n}^+ \cdot \mathbf{C}^*_m : \left[\mathbb{I} + \boldsymbol{\mathcal{E}}_y(\boldsymbol{\xi}^+)\right] & = & \mathbf{n}^+ \cdot \mathbf{C}^*_m : \left[\mathbb{I} + \boldsymbol{\mathcal{E}}_y(\boldsymbol{\xi}^-)\right] & \\ & = & K_n[\![\boldsymbol{\xi}_n]\!] + K_\tau[\![\boldsymbol{\xi}_\tau]\!] & \text{on } \partial Y_{mf} \end{array}\right. \tag{72}$$

with $[\![\boldsymbol{\xi}_n]\!] = \mathbf{n}^+ \left(\mathbf{n}^+ \cdot \boldsymbol{\xi}^+ + \mathbf{n}^- \cdot \boldsymbol{\xi}^-\right)$ and $[\![\boldsymbol{\xi}_\tau]\!] = \boldsymbol{\xi}^+ - \boldsymbol{\xi}^- - [\![\boldsymbol{\xi}_n]\!]$. Thus, defining the total macroscopic stress $\boldsymbol{\sigma}_T^{(0)}$ as the average of $\boldsymbol{\sigma}_m^{(0)}$ ($\boldsymbol{\sigma}_T^{(0)} = \langle \boldsymbol{\sigma}_m^{(0)} \rangle$), by integrating (66d) over Y and using (71) and (66) gives

$$\boldsymbol{\nabla}_x \cdot \mathrm{d}\boldsymbol{\sigma}_T^{(0)} = 0$$

where

$$\mathrm{d}\boldsymbol{\sigma}_T^{(0)} = \mathbb{C}^{eff} : \boldsymbol{\mathcal{E}}_x(\mathrm{d}\mathbf{u}^{(0)}) + \langle \mathbf{C}_m^* : \boldsymbol{\mathcal{E}}_y(\mathrm{d}\mathbf{u}_\pi^{(1)}) \rangle - \sum_{i=1}^{N} \boldsymbol{\alpha}_{m,i}^* \, \mathrm{d}p_{f,i}^{(0)} \tag{73}$$

with the three-scale effective elasticity tensor inheriting the same dependence on $\boldsymbol{\xi}$ of the two-scale problem

$$\mathbb{C}^{eff} \quad = \quad \mathbf{C}_m^* : \left\langle \left[\mathbb{I} + \boldsymbol{\mathcal{E}}_y(\boldsymbol{\xi}) \right] \right\rangle \tag{74}$$

which brings extra dependence on fluid pressure through the BB-dependent $\boldsymbol{\xi}$. Equation (73) consists of the incremental form of the macroscopic effective stress principle. It is remarkable to see that, in contrast to the linear poroelastic case, solvation forces do not limit the fluid pressure effects to the Biot-Willis term but also affect the effective stress.

We are now left to compute perturbations in the volume fraction of the cleats $d\phi_{cleat}$ induced by pore pressure changes. To this end, we begin by computing variations in the cleat aperture profile $H(\boldsymbol{y})$ which is engendered by the jump of the normal fluctuation displacements $\mathbf{u}^{(1)}$. From (71) this yields

$$\mathrm{d}H = \mathbf{n}^+ \cdot [\![\boldsymbol{\xi}]\!] : \boldsymbol{\mathcal{E}}_x(\mathrm{d}\mathbf{u}^{(0)}) + \mathbf{n}^+ \cdot [\![\mathrm{d}\mathbf{u}_\pi^{(1)}]\!] \tag{75}$$

with

$$\begin{aligned} [\![\boldsymbol{\xi}]\!] &= \boldsymbol{\xi}^{+} - \boldsymbol{\xi}^{-} \\ [\![\mathrm{d}\mathbf{u}_{\pi}^{(1)}]\!] &= \mathrm{d}\mathbf{u}_{\pi}^{(1)+} - \mathrm{d}\mathbf{u}_{\pi}^{(1)-} \end{aligned} \tag{76}$$

306 Hence, integration over the cleat/matrix interface ∂Y_{mf} within each cell furnishes

$$\mathrm{d}\phi_{cleat} = \frac{1}{|Y|}\int_{\partial Y} \mathrm{d}H \, \mathrm{d}\Gamma \tag{77}$$

307 Thus, by combining the above results we have from the divergence theorem and periodicity

$$\mathrm{d}\phi_{cleat} = -\left[\left\langle \boldsymbol{\nabla}_y \cdot \boldsymbol{\xi} \right\rangle : \boldsymbol{\mathcal{E}}_x\left(\mathrm{d}\mathbf{u}^{(0)}\right) + \left\langle \boldsymbol{\nabla}_y \cdot \mathrm{d}\mathbf{u}_{\pi}^{(1)} \right\rangle\right] \tag{78}$$

308 The above incremental relation provides the desired result for any nanopore geometry.

309 3.4.3 Application to spherical-nanopore geometry

310 The aforementioned isotropic representation for the solvation force also allows to simplify the three-
311 scale closure relations for the poromechanical coefficients. In a similar fashion to the local problem
312 (72) for the third-order characteristic function $\boldsymbol{\xi}$, we introduce the three-scale vectorial function $\boldsymbol{\eta}$.

$$\begin{cases} \boldsymbol{\nabla}_y \cdot \left[\mathbf{C}_m^{*} : \boldsymbol{\mathcal{E}}_y(\boldsymbol{\eta})\right] = 0 & \text{in } Y_m \\ \mathbf{C}_m^{*} : \boldsymbol{\mathcal{E}}_y(\boldsymbol{\eta}^{+}) \cdot \mathbf{n}^{+} = \mathbf{C}_m^{*} : \boldsymbol{\mathcal{E}}_y(\boldsymbol{\eta}^{-}) \cdot \mathbf{n}^{+} & \\ \qquad\qquad = K_n [\![\boldsymbol{\eta}_n]\!] + K_\tau [\![\boldsymbol{\eta}_\tau]\!] - \mathbf{n}^{+} & \text{on } \partial Y_{mf} \end{cases} \tag{79}$$

313 with $[\![\boldsymbol{\eta}_n]\!] = \mathbf{n}^{+}\left(\mathbf{n}^{+} \cdot \boldsymbol{\eta}^{+} + \mathbf{n}^{-} \cdot \boldsymbol{\eta}^{-}\right)$ and $[\![\boldsymbol{\eta}_\tau]\!] = \boldsymbol{\eta}^{+} - \boldsymbol{\eta}^{-} - [\![\boldsymbol{\eta}_n]\!]$. Under the spherical representation for
314 the scalar $\alpha_{m,i}^{*}$ in (59), we can explore the above definition along with the linearity in (70) to reduce

(71) to the form

$$\mathrm{d}\mathbf{u}^{(1)} = \boldsymbol{\xi} : \boldsymbol{\mathcal{E}}_x(\mathrm{d}\mathbf{u}^{(0)}) + \boldsymbol{\eta} \sum_{i=1}^{N} (\alpha_f - \alpha^*_{m,i})\, \mathrm{d}p^{(0)}_{f,i} \tag{80}$$

In addition, the reduced representation for $\mathbf{u}^1_\pi$ in the last term in r.h.s can be combined with (73) to infer for the total stress

$$\mathrm{d}\boldsymbol{\sigma}^{(0)}_T \;=\; \mathbb{C}^{eff} : \boldsymbol{\mathcal{E}}_x(\mathrm{d}\mathbf{u}^{(0)}) - \sum_{i=1}^{N} \left[\overline{\boldsymbol{\alpha}}(\alpha_f - \alpha^*_{m,i}) + \alpha^*_{m,i}\mathbf{I}\right] \mathrm{d}p^{(0)}_{f,i} \tag{81}$$

with

$$\overline{\boldsymbol{\alpha}} \;:=\; -\left\langle \mathbf{C}^*_m : \boldsymbol{\mathcal{E}}_y(\boldsymbol{\eta}) \right\rangle = -\left\langle \boldsymbol{\nabla}_y \cdot \boldsymbol{\xi} \right\rangle \tag{82}$$

The last equality between the characteristic functions $\boldsymbol{\eta}$ and $\boldsymbol{\xi}$ is well established in the traditional context of poroelasticity where it leads to symmetry in the governing equations (see e.g. [32]). The extension of such property to the present more complex case, with underlying dependence on the BB-stiffness, requires further elaboration (see A).

The fluid pressure dependent macroscopic effective stress is defined as

$$\boldsymbol{\sigma}^{(0)}_{eff} := \mathbb{C}^{eff} : \boldsymbol{\mathcal{E}}_x(\mathrm{d}\mathbf{u}^{(0)}) \tag{83}$$

whereas the Biot-Willis parameter reads as

$$\begin{aligned} \boldsymbol{\alpha}^T_i : \;&=\; \overline{\boldsymbol{\alpha}}(\alpha_f - \alpha^*_{m,i}) + \alpha^*_{m,i}\mathbf{I} \\ &=\; \underbrace{\alpha_f \overline{\boldsymbol{\alpha}} + \alpha_m\,(\mathbf{I} - \overline{\boldsymbol{\alpha}})}_{\text{Non-linear poroelasticity}} \underbrace{-\,(\gamma_i + \nu\beta_i)\,(\mathbf{I} - \overline{\boldsymbol{\alpha}})}_{\text{Solvation effects}} \end{aligned} \tag{84}$$

The above underlying decomposition suggests the additive sum of the effects stemming from poroelasticity in conjunction with the BB effects in the cleats, and the contribution arising from the solvation force. In particular, unlike poroelasticity, the magnitude of the latter swelling component is not constrained to unitary interval.

Finally, we address the modeling of the perturbations in cleat porosity $H(\boldsymbol{y})$ induced by increment in pore pressure. By incorporating the jumps in the decomposition (80) for the displacement fluctuations we have

$$\mathrm{d}H \;=\; \mathbf{n}^{+}\cdot[\![\boldsymbol{\xi}]\!]:\boldsymbol{\mathcal{E}}_x(\mathrm{d}\mathbf{u}^{(0)})+\mathbf{n}^{+}\cdot[\![\boldsymbol{\eta}]\!]\sum_{i=1}^{N}(\alpha_f-\alpha^{*}_{m,i})\mathrm{d}p^{(0)}_{f,i} \tag{85}$$

which by the divergence theorem leads to the incremental cleat volume fraction ϕ_{cleat} given by

$$\begin{aligned}\mathrm{d}\phi_{cleat} &= -\left[\left\langle\boldsymbol{\nabla}_y\cdot\boldsymbol{\xi}\right\rangle:\boldsymbol{\mathcal{E}}_x\left(\mathrm{d}\mathbf{u}^{(0)}\right)+\left\langle\boldsymbol{\nabla}_y\cdot\boldsymbol{\eta}\right\rangle\sum_{i=1}^{N}\left(\alpha_f-\alpha^{*}_{m,i}\right)\mathrm{d}p^{(0)}_{f,i}\right]\\ &= \overline{\boldsymbol{\alpha}}:\boldsymbol{\mathcal{E}}_x\left(\mathrm{d}\mathbf{u}^{(0)}\right)-\left\langle\boldsymbol{\nabla}_y\cdot\boldsymbol{\eta}\right\rangle\sum_{i=1}^{N}\left(\alpha_f-\alpha^{*}_{m,i}\right)\mathrm{d}p^{(0)}_{f,i}\end{aligned} \tag{86}$$

When compared to the more general constitutive law (78), the above result explores the linear decomposition underlying $\mathbf{u}^{(1)}_{\pi}$ to obtain a reduced representation.

3.5 Summary of three-scale poromechanical model

We are now in position of stating the three-scale poromechanical model in the case of spherical nanopores. Given the set of parameters $\{\mathbf{c}_s,\boldsymbol{\alpha}_m,\phi^{ref}_m,k_s,\boldsymbol{\gamma}_i,\boldsymbol{\nu}\}$ for the coal matrix, compute the homogenized parameters $\{\mathbf{C}^{*}_m,\boldsymbol{\alpha}^{*}_{m,i},\beta_i\}$ by invoking the two-scale closure relations (25), (50), and (62).

Further, given the pair of BB-stiffness $\{K_n,K_\tau\}$, solve (72) and (79) for the pressure-dependent characteristic functions $\boldsymbol{\xi}$ and $\boldsymbol{\eta}$ and (82) and for $\overline{\boldsymbol{\alpha}}$. Our three-scale incremental poromechanical

model consists in, given the values of the macroscopic poromechanical variables at the reference configuration along with the perturbations in the fluid pressure field of each gas $p_{f,i}^{(0)}$, compute the the triplet increments $\{\mathrm{d}\boldsymbol{\sigma}_T^{(0)}, \mathrm{d}\mathbf{u}^{(0)}), \mathrm{d}\phi_{cleat}\}$ satisfying

$$\begin{cases} \boldsymbol{\nabla}_x \cdot \mathrm{d}\boldsymbol{\sigma}_T^{(0)} = 0 \\ \mathrm{d}\boldsymbol{\sigma}_T^{(0)} = \mathbb{C}^{eff} : \boldsymbol{\mathcal{E}}_x(\mathrm{d}\mathbf{u}^{(0)}) - \sum_{i=1}^{N} \boldsymbol{\alpha}_i^T \, \mathrm{d}p_{f,i}^{(0)} \\ \mathrm{d}\phi_{cleat} = \overline{\boldsymbol{\alpha}} : \boldsymbol{\mathcal{E}}_x \left(\mathrm{d}\mathbf{u}^{(0)}\right) - \left\langle \boldsymbol{\nabla}_y \cdot \boldsymbol{\eta} \right\rangle \sum_{i=1}^{N} \left(\alpha_f - \alpha_{m,i}^*\right) \mathrm{d}p_{f,i}^{(0)} \end{cases}$$

with the homogenized coefficients $\{\mathbb{C}^{eff}, \boldsymbol{\alpha}_i^T\}$ given by (74 and (84).

Note that for a non-porous matrix ($\alpha_m \simeq 0$), in the absence of solvation force effects ($\gamma_i = \nu \simeq 0$) and a Biot coefficient of the cleats $\alpha_f = 1$, the symmetry of the Biot relations is recovered:

$$\mathrm{d}\boldsymbol{\sigma}_T^{(0)} = \mathbb{C}^{eff} : \boldsymbol{\mathcal{E}}_x(\mathrm{d}\mathbf{u}^{(0)}) - \overline{\boldsymbol{\alpha}} \, \mathrm{d}p_f^{(0)} \tag{87}$$

$$\mathrm{d}\phi_{cleat} = \overline{\boldsymbol{\alpha}} : \boldsymbol{\mathcal{E}}_x \left(\mathrm{d}\mathbf{u}^{(0)}\right) - \left\langle \boldsymbol{\nabla}_y \cdot \boldsymbol{\eta} \right\rangle \mathrm{d}p_f^{(0)} \tag{88}$$

4 Computational Simulations

Hereafter we present numerical experiments of the constitutive response of the homogenized coefficients along with preliminary simulations of a CO_2 injection in a coalbed methane reservoir.

4.1 Two-scale coefficients for the coal matrix

We begin by presenting the numerical results for the two-scale problem by quantifying the effects of the solvation force upon the magnitude of the homogenized coefficients in the coal matrix. In the simulations that follow, we consider the periodic cell with a single nanopore at the center with a given matrix porosity ϕ_m and pore radius R filled by CO_2. To simplify notation, the single subscript

$i = CO_2$ is hereafter omitted. In addition, for a given matrix porosity ϕ_m the traditional poromechanical constant values are assessed using Mori-Tanaka approach [34].

The input data for the simulations that follow are shown in Table 1. Particularly, the pair of elastic parameters of the solid phase $\{v_s, k_s\}$ are typically selected within the range of values for a coal matrix (see [35]). Our first target is to quantify the sensitivity of the solvation force with changes in pressure p_m which is dictated by the coefficient γ. In Figure 6a we display the behavior of γ with changes in

Parameters	Unit	Value
Temperature T	K	318
Molecular diameter d_{CO_2}	m	3.9×10^{-10}
Pore diameter $D_p = 2\,R$	m	$5\,d_{CO_2}$
Reference bulk pressure p_m^{ref}	MPa	0.5
Bulk modulus of solid phase k_s	GPa	4.5
Poisson coefficient of solid phase v_s		0.4
Reference matrix porosity ϕ_m	%	18.5
Biot coefficient of matrix α_m		0.5
Young's modulus of matrix E_m	GPa	1.86
Poisson's ratio of matrix v_m		0.36

Table 1: Parameters used in numerical simulations of the two-scale parameters.

the CO_2 pressure. We may observe initially a sharp decrease stemming from the abrupt appearance of attractive forces followed by a gradual increase as the effects of the solvation force tend to diminish with the increase in gas pressure. Such a latter behavior induces swelling of the matrix blocks leading to the closure of the cleats. Further, by invoking (50), the aforementioned behavior in γ engenders perturbations in the magnitude of the modified Biot coefficient of the matrix as shown in Figure 6b . It is remarkable to see the tremendous increase in α_m^* for low pressure values which allows the coal matrix to sustain substantial increase in gas pressure during CO_2 injection. After reaching the peak, the effects of the solvation force tend to decrease in the range of high gas pressure leading to a decrease in α_m^* but nevertheless still bigger than unit, which is commonly envisioned as an upper bound in traditional poroelasticity.

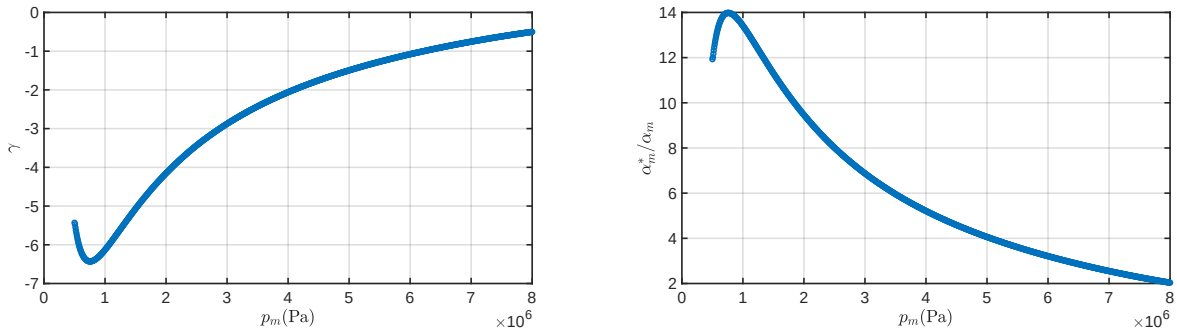

(a) (b)

Figure 6: Dependence of γ (a); and α_m^*/α_m (b) on the CO_2 pressure.

We display the bulk modulus $9K_m^* := \mathbf{C}_m^* : \mathbf{I} : \mathbf{I}$ as a function of the pore diameter parametrized by the gas pressure. By comparing the microscopic representations (50) and (49), we may observe that, unlike α_m^*, which is highly sensitive to γ_i, the profiles of K_m^* show weaker dependence on both pore diameter and gas pressure as depicted in Figure 7. The dependence of the ratio K_m^*/K_m with increase in pore size shows mild deviations from the unit value, which suggests adopting the approximation $\mathbf{C}_m^* \simeq \mathbf{C}_m$ in the subsequent simulations. In addition, owing to the volumetric influence of the solvation force in the isotropic scenario, from (59) the modified Lamé's second parameter μ_m^* remains insensitive to solvation effects.

Finally, the two-scale poromechanical model is illustrated in a canonical swelling example induced by CO_2 injection. Our selected scenario comprises a coal sample immersed in a chamber filled by CO_2 at thermodynamic equilibrium under an homogeneous bulk pressure, which is increased quasi-statically and parametrized by a sequence of equilibrium states. Input parameters are shown in Table 1. In Figure 8, we display the dependence of the volumetric strain of the coal sample according with the CO_2 bulk pressure. As expected, rapid increase of the volumetric strain dominates at low pressure tending asymptotically to a plateau at high pressures owing to the attenuation of the solvation force.

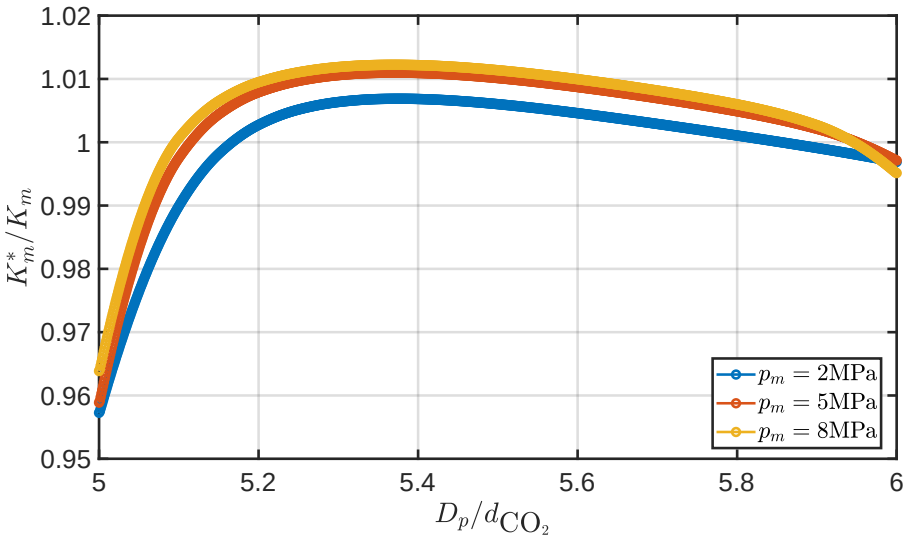

Figure 7: Dependence of K_m^*/K_m on the pore diameter for different values of the CO_2 pressure.

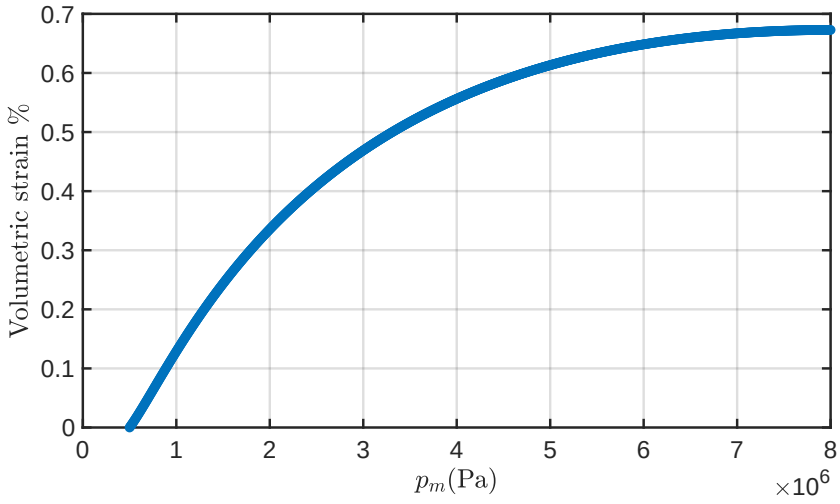

Figure 8: Volumetric strain vs CO_2 bulk pressure

4.2 Three-scale poromechanical parameters

We now proceed towards the computation of the three-scale poromechanical parameters, whose magnitude now incorporates the non-linear BB-stiffness $\{K_n, K_\tau\}$ inherent to the cleat system. Our simulations are carried out for the two cell configurations depicted in Figure 9, based on a simple cross arrangement and two face/butt cleats [4]. We remark that, in spite of selecting simple cell-geometries,

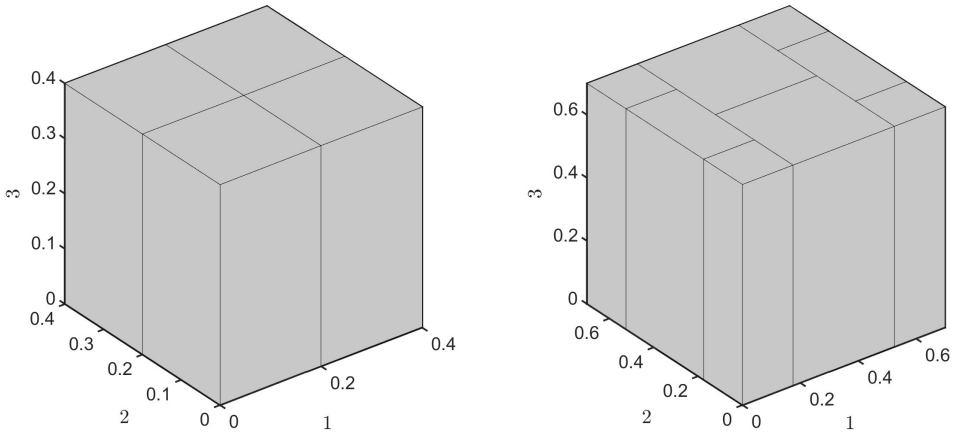

(a) Cell type 1 (b) Cell type 2

Figure 9: Cell configurations exhibiting cross arrangement and face/butt cleats

the upscaling may lead to a highly anisotropic medium induced by the distinct properties between the two orthogonal cleat families (see B). In addition, the tangential cleat stiffness K_τ usually exhibits a different constitutive response compared to the normal counterpart K_n leading to additional sources of anisotropy. For the sake of simplicity, the cleat parameters are suitably chosen in order to enforce transverse isotropy of the homogenized medium (see Table 2). The other parameters associated with the matrix are presented in Table 1.

Both configurations in Figure 9 have the same initial cleat porosity and BB-stiffness parameters. The geometry is chosen to ensure the continuity of the cleat network. Periodic conditions are imposed on the boundaries. For cell 1, the auxiliary problems (72) and (79) admit the analytical solutions

Parameters	Unit	Value
Initial normal stiffness K_{ni} [36]	GPa/m	6.6
Initial tangential stiffness $K_{\tau i}$ [36]	GPa/m	6.6
Initial aperture V_m [36]	m	107×10^{-6}
Reference normal stiffness K_n^{ref}	GPa/m	1111
Reference tangential stiffness K_τ^{ref}	GPa/m	6.6
Reference aperture V_m^{ref}	m	8.25×10^{-6}
Cleat porosity at reference ϕ_{cleat}^{ref}	%	0.41

Table 2: Parameters used in numerical simulations for the cleats.

given in B and C. Due to the complexity of the cleat network in the cell 2, calculations are performed numerically using the Structural Mechanics Module implemented in COMSOL Multiphysics software.

In Figure 10 we plot the horizontal ($\alpha_{11}^T = \alpha_{22}^T$) and vertical ($\alpha_{33}^T$) components of the macroscopic Biot-Willis coefficient as a function of the gas pressure for cell type-1. Firstly, α^T augments in magnitude due to the increase of the solvation force for low pressures, reaching a peak in the vicinity of the value of 1 MPa, and subsequently followed by a gradual decrease as the solvation force tends to diminish with the CO_2 pressure build-up. In addition, the cleat closure driven by the raise in pressure increases the stiffness of the fractured coal matrix, as shown in Figure 10b which displays the evolution of the horizontal stiffness C_{1111}^{eff} with the gas pressure.

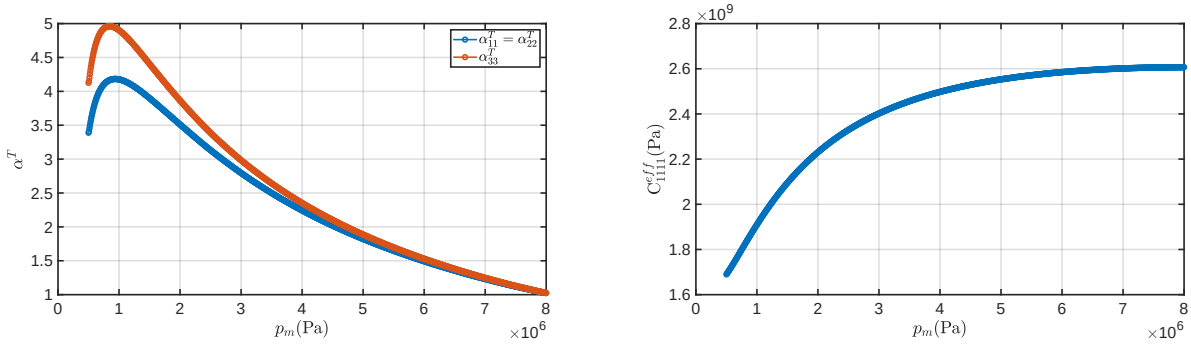

(a) (b)

Figure 10: Dependence of (a) α^T and (b) $\mathbb{C}_{1111}^{eff}$ on the gas pressure

We now analyze the effects of the cell geometry on cleat porosity. Considering both arrangements

in Figure 9, in Figure 11 we display the dependence of cleat closure on the gas pressure. Despite both cells exhibiting strong dissimilarities in local geometry, we observe minor differences between the two arrangements for a wide-range of pore pressures. Such a result motivates the use of a simple type 1 cell to reproduce patterns commonly encountered in more complex geometries.

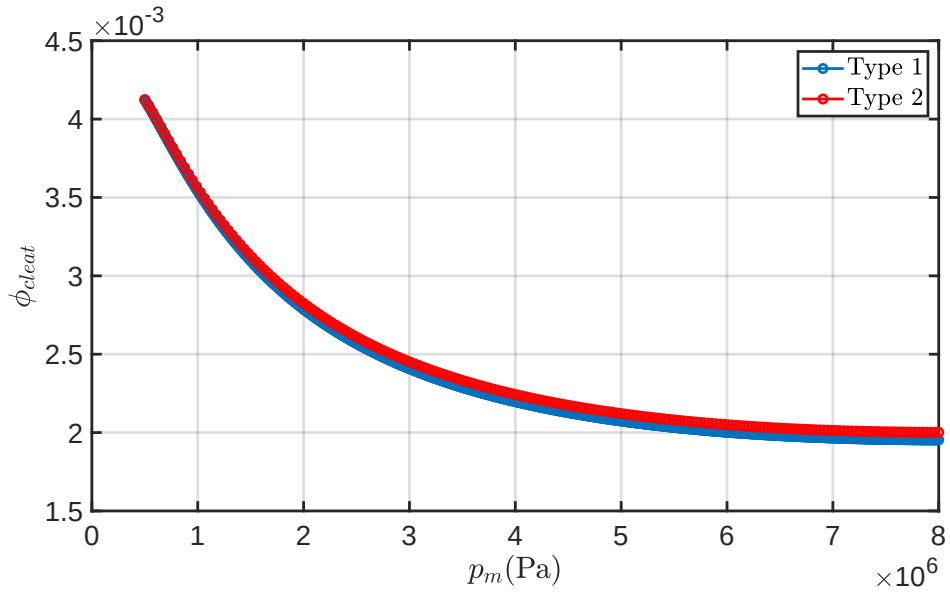

Figure 11: Decrease of ϕ_{cleat} with CO_2 pressure buid-up for two cell configurations

4.3 Macroscopic example of CO_2 injection

We now illustrate the performance of the three-scale model proposed herein in a macroscopic example of CO_2 sequestration. The sketch in Figure 12 shows two injection wells located at opposite corners of the reservoir. The calculations are performed in a 100 m x 100 m x 2 m (sugar-box reservoir). Our subsequent calculations are carried out in COMSOL Multiphysics software, considering zero displacement at the external boundaries, so that matrix and cleats interchange the perturbations in strain. The input parameters used in the simulations are listed in Table 1 and Table 2.

It should be noted that the full coupling between hydrodynamics and poromechanics is not con-

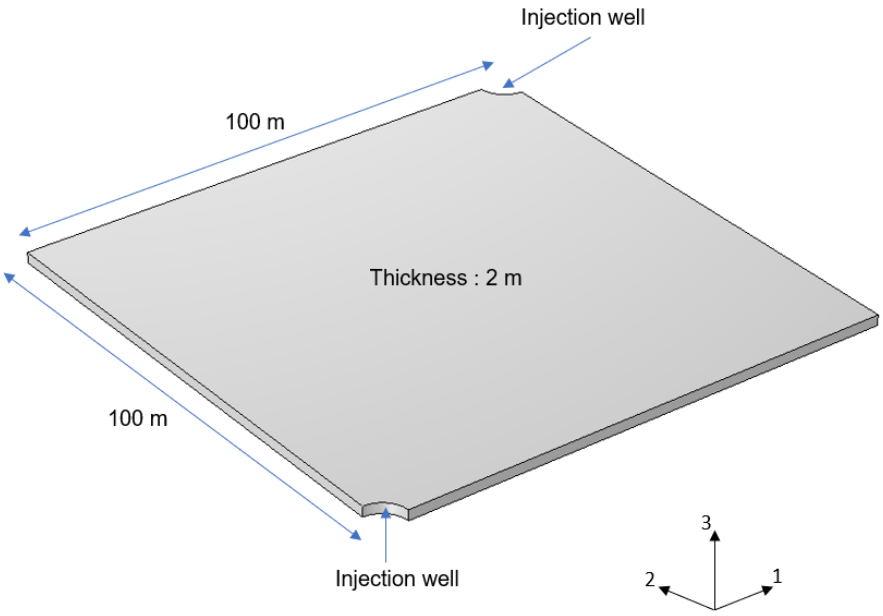

Figure 12: Sketch of the macroscopic example of CO_2 injection

sidered in this work. Hence, the input pressure evolving profiles shown in Figure 13 are assumed solution of a linear diffusion equation at some discrete times considering initial and well pressures $p_f(t = 0) = 0.5$ MPa and $p_f = 8$ MPa respectively. In regards to the boundary conditions for the flow problem, Dirichlet conditions for the pressure are enforced at the wells combined with no-flux conditions at the edges of the reservoir. The horizontal component profile of $\boldsymbol{\alpha}^T_{11}$ is shown in Figure 14 for two times. We can observe a peak in four orders of magnitude for low pressure values compared to the unit of incompressible poroelasticity. The pressure build-up tends to further reduce the magnitude particularly propagating from the injection wells. For large times, lower and higher values of the horizontal component of $\boldsymbol{\alpha}^T$ tend to clusterize in the vicinity of the injectors and in the center of the reservoir respectively.

Figure 15 and Figure 16 depict the variability of the macroscopic stiffness $\mathbb{C}^{eff}_{1111}$ and cleat porosity ϕ_{cleat}. Near the injection well, in contrast to non-swelling media, the cleat porosity decreases counter-intuitively implying in strong decrease in permeability and increase in macroscopic stiffness induced

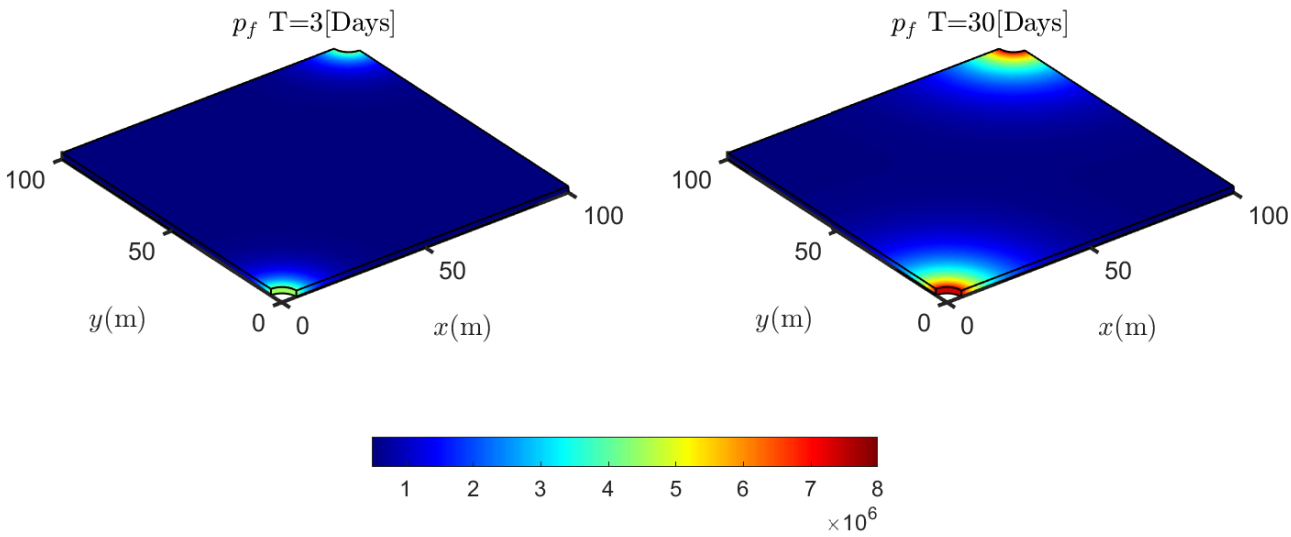

Figure 13: Input CO_2 pressure profiles in the reservoir, computed from a simple diffusion equation for different times

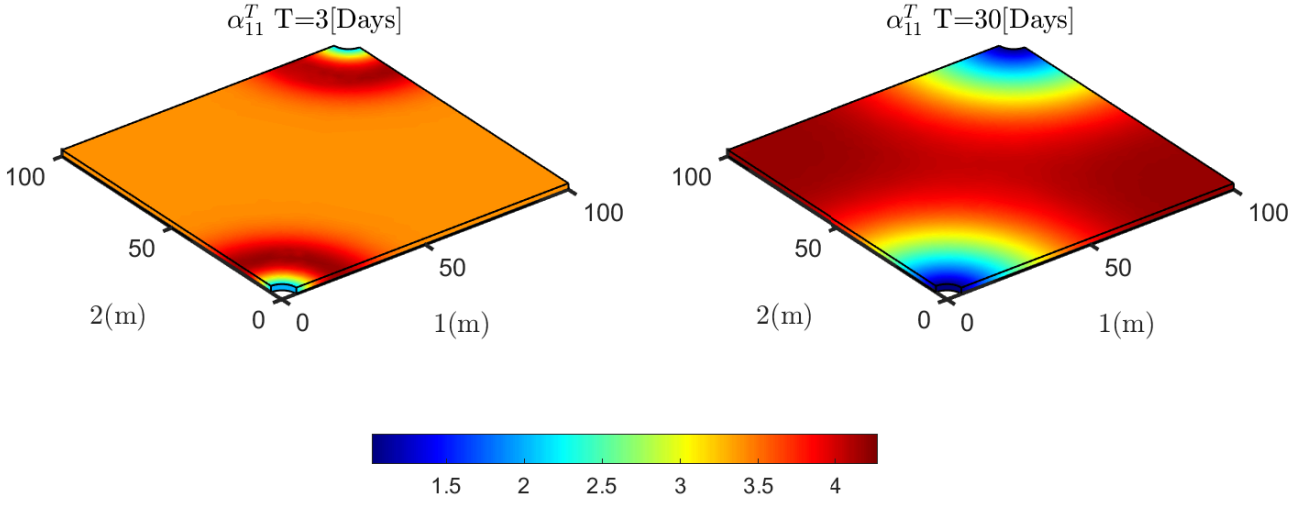

Figure 14: Variability of α_{11}^T for different times

by matrix swelling. Subsequently, as time and gas pressure increase, such a low porosity sub-region is propagated towards the center of the reservoir mainly through the diagonal connecting the two injection wells and afterwards spreading to other locations. It is remarkable to see the essential role played by the non-linear Barton-Bandis law to counterbalance the cleat closure due to matrix swelling. The non-linear behavior of the stress in the cleat network is crucial to preserve residual values of the cleat porosity consequently avoiding interpenetration of adjacent matrix blocks.

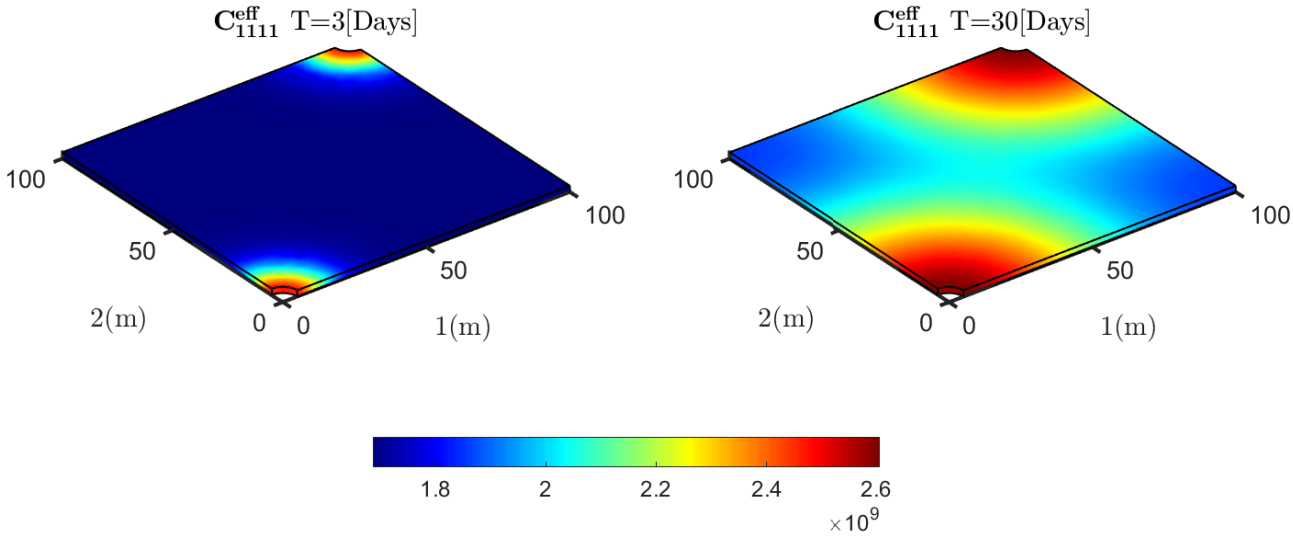

Figure 15: Variability of $\mathbb{C}^{eff}_{1111}$ for different times

5 Conclusions

We developed an innovative three-scale poromechanical model for coalbed methane reservoirs composed of the coal matrix containing nanopores intertwined by a network of lower dimensional cleats saturated by a gas mixture. By exploring the DFT approach, the solvation force induces modified effective stress principle including the effects of the attractive solvation forces. Within the framework of the incremental formulation, the effects of the solvation force are mainly manifested in a modified Biot-Willis parameter with magnitude dictated by the sensitivity of the solvation force with changes

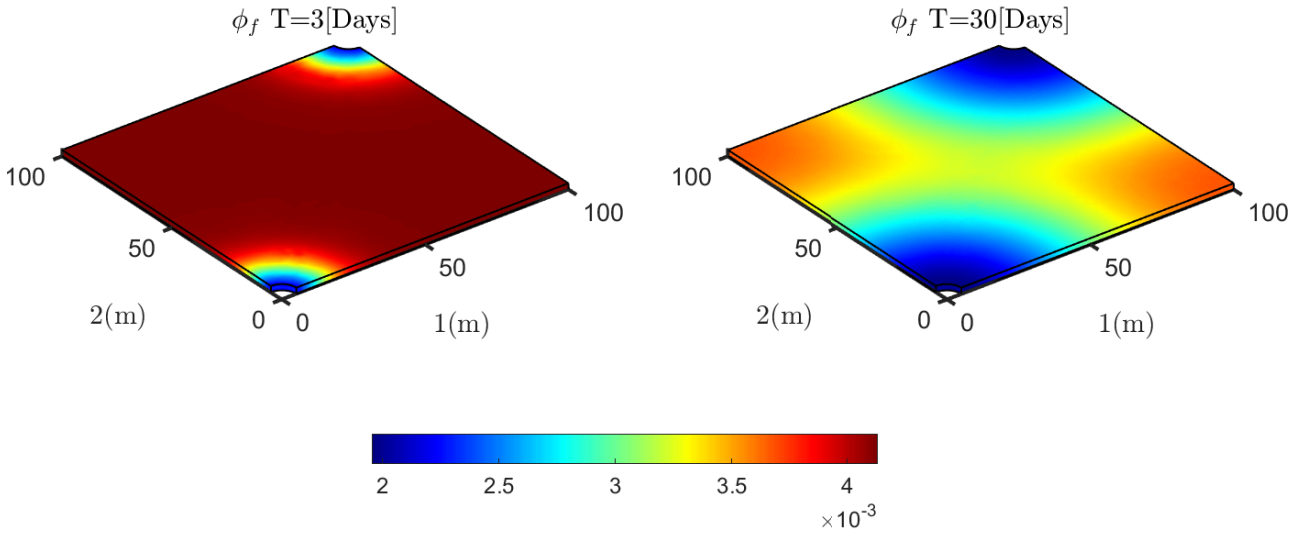

Figure 16: Variability of ϕ_{cleat} for different times

in gas pressure. In particular, at low pressures, we observed a tremendous increase in $\alpha^*_{m,i}$ which may achieve up to ten times the unit value of classical poroelasticity. Such a non-intuitive pattern suggests that, for a fixed reservoir volume, small variations in the pressure in the cleats may imply in large variations in total stress of the matrix.

In contrast to previous approaches, the cleat system is supposed to withstand normal and tangential stresses, which act to counterbalance the effects of the solvation force in the matrix blocks. By postulating a non-linear hyperbolic law in the sense of Barton and Bandis for the normal stress, within the framework of reiterated homogenization, the role of the BB component is manifested in the profile of the characteristic functions. In this context, the increase in the normal BB-stiffness of the cleats tends to reduce the jumps of these functions at the matrix/cleat interfaces which are propagated to the macroscale in terms of perturbations in the macrocoscopic poromechanical parameters.

In addition to the overall three-scale decomposition of the total macroscopic stress, we constructed a new constitutive law for the Lagrangian cleat porosity. Moreover, a new undrained-type coefficient naturally arises in the constitutive response of the cleat porosity which plays a central role in the cleat permeability response. The dependence of the two- and three-scale homogenized poromechanical

coefficients on the gas pressure is reconstructed numerically quantifying precisely the influence of the solvation force.

To the authors best knowledge, the paper is the first attempt to address the important mechanical interaction between solvation force and BB restoring stresses in nanoporous jointed rocks. Ongoing work will incorporate the full coupling with the flow equations in the cleat system.

Acknowledgement

The authors would like to thank the EXPLOR center of the University of Lorraine for providing the computer resources necessary to perform the numerical simulations. Q D Ha also thanks the 'Grand Est' Region for the research grant allowing him to carry out his PhD thesis.

A Proof of Symmetry

In the classical poromechanics, it has been proved that [32]

$$\langle \boldsymbol{\nabla} \cdot \boldsymbol{\xi} \rangle \;=\; \langle \boldsymbol{\sigma}\,(\boldsymbol{\eta}) \rangle \tag{89}$$

The aim of this appendix is to verify this relation in the case of non-linear BB law for the mechanical behavior of the cleats.

$\boldsymbol{\xi}$ is a third-order tensor. If the two last indices p and q are kept fixed, from (72), by using tensor notation the problem for the vector $\boldsymbol{\xi}^{pq}$ is written as

$$\left\{\begin{array}{rcll} \dfrac{\partial}{\partial y_j}\left[\mathrm{C}^*_{ijkl}\,\mathcal{E}_{kl}(\boldsymbol{\xi}^{pq})\right] & = & 0 & \text{in } Y_m \\ \mathrm{C}^*_{ijkl}\,\left[\mathcal{E}_{kl}\left(\boldsymbol{\xi}^{pq+}\right)+\delta_{kp}\,\delta_{lq}\right]n^+_j & = & \mathrm{C}^*_{ijkl}\,\left[\mathcal{E}_{kl}\left(\boldsymbol{\xi}^{pq-}\right)+\delta_{kp}\,\delta_{lq}\right]n^+_j & \\ & = & K_n[\![\xi^{pq}_i]\!]_n + K_\tau[\![\xi^{pq}_i]\!]_\tau & \text{on } \partial Y_{fm} \end{array}\right. \tag{90}$$

with $[\![\boldsymbol{\xi}^{pq}]\!]_n = \mathbf{n}^+ \left(\mathbf{n}^+ \cdot \boldsymbol{\xi}^{pq+} + \mathbf{n}^- \cdot \boldsymbol{\xi}^{pq-}\right)$ and $[\![\boldsymbol{\xi}^{pq}]\!]_\tau = \boldsymbol{\xi}^{pq+} - \boldsymbol{\xi}^{pq-} - [\![\boldsymbol{\xi}^{pq}]\!]_n$ where the indices n and τ designates respectively the normal and the tangential component of the jump of $\boldsymbol{\xi}^{pq}$ on the two faces $\pm$ of the cleat (see Figure 4).

The problem for the vector $\boldsymbol{\eta}$ is expressed as

$$\left\{\begin{array}{rcll} \dfrac{\partial}{\partial y_j}\left[\mathrm{C}^*_{ijkl}\,\mathcal{E}_{kl}(\boldsymbol{\eta})\right] & = & 0 & \text{in } Y_m \\ \left[\mathrm{C}^*_{ijkl} : \mathcal{E}_{kl}\left(\boldsymbol{\eta}^+\right) + \delta_{ij}\right] n^+_j & = & \left[\mathrm{C}^*_{ijkl} : \mathcal{E}_{kl}\left(\boldsymbol{\eta}^-\right) + \delta_{ij}\right] n^+_j & \text{on } \partial Y_{fm} \\ & = & K_n [\![\eta_i]\!]_n + K_\tau [\![\eta_i]\!]_\tau & \end{array}\right. \tag{91}$$

with $[\![\boldsymbol{\eta}]\!]_n = \left(\mathbf{n}^+ \cdot \boldsymbol{\eta}^+ + \mathbf{n}^- \cdot \boldsymbol{\eta}^-\right) \mathbf{n}^+$ and $[\![\boldsymbol{\eta}]\!]_\tau = \boldsymbol{\eta}^+ - \boldsymbol{\eta}^- - [\![\boldsymbol{\eta}]\!]_n$.

The cleat network splits the matrix Y_m into M sub-domains Y_{m_α} with $1 \leq \alpha \leq M$. For any Y-periodic displacement field $\mathbf{u}$ satisfying on each part Y_{m_α} of the unit cell, $\boldsymbol{\nabla} \cdot \boldsymbol{\sigma}(\mathbf{u}) = 0$ and for any Y-periodic vector $\boldsymbol{\omega}$ differentiable on each part Y_{m_α}, we have (noting that the normal exterior to Y_{m_α} on $\partial Y^{\pm}_{m_\alpha}$ is $\mathbf{n}^{\mp}$)

$$\begin{aligned} 0 &= \int_{Y_m} \frac{\partial \sigma_{ij}(\mathbf{u})}{\partial y_j}\,\omega_i \,\mathrm{d}V = \sum_\alpha \int_{Y_{m\alpha}} \frac{\partial \sigma_{ij}(\mathbf{u})}{\partial y_j}\,\omega_i \,\mathrm{d}V \\ &= \sum_\alpha \int_{\partial Y^-_{m\alpha}} \sigma_{ij}(\mathbf{u})\,\omega_i^-\, n_j^+ \,\mathrm{d}S + \sum_\alpha \int_{\partial Y^+_{m\alpha}} \sigma_{ij}(\mathbf{u})\,\omega_i^+\, n_j^- \,\mathrm{d}S - \sum_\alpha \int_{Y_{m\alpha}} \sigma_{ij}(\mathbf{u})\,\frac{\partial \omega_i}{\partial y_j}\,\mathrm{d}V \\ &= -\sum_\alpha \int_{\partial Y_{m\alpha}} \sigma_{ij}(\mathbf{u})\,[\![\omega_i]\!]\, n_j^+ \,\mathrm{d}S - \sum_\alpha \int_{Y_{m\alpha}} \sigma_{ij}(\mathbf{u})\,\frac{\partial \omega_i}{\partial y_j}\,\mathrm{d}V \end{aligned} \tag{92}$$

with $\partial Y^+_{m_\alpha} \equiv \partial Y^-_{m_\alpha}$ and $[\![\boldsymbol{\omega}]\!] = \boldsymbol{\omega}^+ - \boldsymbol{\omega}^-$.

Finally using the symmetry of $\boldsymbol{\sigma}(\mathbf{u}) = \mathbf{C}^* : \boldsymbol{\mathcal{E}}(\mathbf{u})$ gives

$$\sum_\alpha \int_{Y_{m\alpha}} \mathrm{C}^*_{ijkl}\,\mathcal{E}_{kl}(\mathbf{u})\,\mathcal{E}_{ij}(\boldsymbol{\omega})\mathrm{d}V = -\sum_\alpha \int_{\partial Y^+_{m\alpha}} \sigma_{ij}(\mathbf{u})\,[\![\omega_i]\!]\, n_j^+ \,\mathrm{d}S \tag{93}$$

Applying the preceding relation for $\mathbf{u} = \boldsymbol{\eta}$ and $\boldsymbol{\omega} = \boldsymbol{\xi}^{pq}$, using the boundary condition (91) on ∂Y_{fm},

the orthogonality of the normal and tangential components, the divergence theorem and the periodicity, we have

$$\begin{aligned}
&\sum_{\alpha}\int_{Y_{m\alpha}} \mathrm{C}^{*}_{ijkl}\,\mathcal{E}_{kl}(\boldsymbol{\eta})\mathcal{E}_{ij}(\boldsymbol{\xi}^{pq})\;\mathrm{d}V \\
&= -\sum_{\alpha}\int_{\partial Y_{m\alpha}} \left(-n_i^{+} + K_n[\![\eta_i]\!]_n + K_\tau[\![\eta_i]\!]_\tau\right)\left([\![\xi_i^{pq}]\!]_n + [\![\xi_i^{pq}]\!]_\tau\right)\mathrm{d}S \\
&= -\sum_{\alpha}\int_{\partial Y_{m\alpha}} \left(-n_i^{+}[\![\xi_i^{pq}]\!] + K_n[\![\eta_i]\!]_n[\![\xi_i^{pq}]\!]_n + K_\tau[\![\eta_i]\!]_\tau[\![\xi_i^{pq}]\!]_\tau\right)\mathrm{d}S \\
&= -\sum_{\alpha}\int_{Y_{m\alpha}} \frac{\partial \xi_i^{pq}}{\partial y_i}\,\mathrm{d}V - \sum_{\alpha}\int_{\partial Y_{m\alpha}} \left(K_n[\![\eta_i]\!]_n[\![\xi_i^{pq}]\!]_n + K_\tau[\![\eta_i]\!]_\tau[\![\xi_i^{pq}]\!]_\tau\right)\mathrm{d}S
\end{aligned} \tag{94}$$

Exploring the same relation but now with $\mathbf{u} = \boldsymbol{\xi}^{pq}$ and $\boldsymbol{\omega} = \boldsymbol{\eta}$ we obtain

$$\begin{aligned}
&\sum_{\alpha}\int_{Y_{m\alpha}} \mathrm{C}^{*}_{ijkl}\,\mathcal{E}_{kl}(\boldsymbol{\xi}^{pq})\,\mathcal{E}_{ij}\,(\boldsymbol{\eta})\;\mathrm{d}V \\
&= -\sum_{\alpha}\int_{\partial Y_{m\alpha}} \left(-\mathrm{C}^{*}_{ijpq}\,n_j^{+} + K_n[\![\xi_i^{pq}]\!]_n + K_\tau[\![\xi_i^{pq}]\!]_\tau\right)\left([\![\eta_i]\!]_n + [\![\eta_i]\!]_\tau\right)\mathrm{d}S \\
&= -\int_{Y_m} \mathrm{C}^{*}_{ijpq}\,\mathcal{E}_{ij}\,(\boldsymbol{\eta})\;\mathrm{d}V - \sum_{\alpha}\int_{\partial Y_{m\alpha}} \left(K_n[\![\xi_i^{pq}]\!]_n[\![\eta_i]\!]_n + K_\tau[\![\xi_i^{pq}]\!]_\tau[\![\eta_i]\!]_\tau\right)\mathrm{d}S
\end{aligned} \tag{95}$$

Due to the symmetry of the elastic tensor ($\mathrm{C}^{*}_{ijkl} = \mathrm{C}^{*}_{klij}$), the two terms on the l.h.s of (94) and (95) are equal and therefore

$$\begin{aligned}
\int_{Y_m} \frac{\partial \xi_i^{pq}}{\partial y_i}\,\mathrm{d}V &= \int_{Y_m} \mathrm{C}^{*}_{ijpq}\,\mathcal{E}_{ij}\,(\boldsymbol{\eta})\;\mathrm{d}V \\
\left\langle \boldsymbol{\nabla}_y \cdot \boldsymbol{\xi}^{pq} \right\rangle &= \left\langle \sigma_{pq}\,(\boldsymbol{\eta}) \right\rangle
\end{aligned} \tag{96}$$

which is an expected result.

B Analytical solution for the closure problems and effective stiffness tensor

Consider the cleat network immersed in the matrix phase characterized by λ and μ for the cross arrangement shown in Figure 9a. The cleat (I) described by (K_n^I, K_τ^I) is located on $y_1 = \ell/2$ whereas the cleat (II) with (K_n^{II}, K_τ^{II}) is placed on $y_2 = \ell/2$. The goal now is to solve the closure problem (90) with

$$\mathrm{C}^*_{ijkl} = \lambda\delta_{ij}\delta_{kl} + \mu\left(\delta_{ik}\delta_{jl} + \delta_{il}\delta_{jk}\right) \tag{97}$$

$$\mathcal{E}_{kl}(\boldsymbol{\xi}^{pq}) = \frac{1}{2}\left(\frac{\partial \xi_k^{pq}}{\partial y_l} + \frac{\partial \xi_l^{pq}}{\partial y_k}\right) \tag{98}$$

From (74), the effective stiffness tensor reads as

$$\mathbb{C}^{eff}_{ijpq} = \mathrm{C}^*_{ijkl}\left(\delta_{kp}\delta_{lq} + \frac{1}{2}\left\langle\frac{\partial \xi_k^{pq}}{\partial y_l} + \frac{\partial \xi_l^{pq}}{\partial y_k}\right\rangle\right) \tag{99}$$

The interface condition on the matrix-cleat interface for the both cleats is written as

$$\begin{aligned}
&\delta_{1j}\left[\lambda\delta_{ij}\delta_{kl} + \mu\left(\delta_{ik}\delta_{jl} + \delta_{il}\delta_{jk}\right)\right]\left[\delta_{kq}\delta_{lq} + \frac{1}{2}\left(\frac{\partial \xi_k^{pq}}{\partial y_l} + \frac{\partial \xi_l^{pq}}{\partial y_k}\right)\right] \\
&= K_n^I\Delta\xi_1^{pq}\delta_{i1} + K_\tau^I\Delta\xi_2^{pq}\delta_{i2} + K_\tau^I\Delta^I\xi_3^{pq}\delta_{i3}
\end{aligned} \tag{100}$$

$$\begin{aligned}
&\delta_{2j}\left[\lambda\delta_{ij}\delta_{kl} + \mu\left(\delta_{ik}\delta_{jl} + \delta_{il}\delta_{jk}\right)\right]\left[\delta_{kq}\delta_{lq} + \frac{1}{2}\left(\frac{\partial \xi_k^{pq}}{\partial y_l} + \frac{\partial \xi_l^{pq}}{\partial y_k}\right)\right] \\
&= K_n^{II}\Delta^{II}\xi_2^{pq}\delta_{i2} + K_\tau^{II}\Delta^{II}\xi_1^{pq}\delta_{i1} + K_\tau^{II}\Delta^{II}\xi_3^{pq}\delta_{i3}
\end{aligned} \tag{101}$$

Performing normal projection gives

$$\lambda + 2\mu + \lambda\left(\frac{\partial \xi_1^{11}}{\partial y_1} + \frac{\partial \xi_2^{11}}{\partial y_2} + \frac{\partial \xi_3^{11}}{\partial y_3}\right) + 2\mu\frac{\partial \xi_1^{11}}{\partial y_1} = K_n^I\Delta^I\xi_1^{11} \tag{102}$$

$$\lambda\left(1+\frac{\partial\xi_1^{11}}{\partial y_1}+\frac{\partial\xi_2^{11}}{\partial y_2}+\frac{\partial\xi_3^{11}}{\partial y_3}\right)+2\mu\frac{\partial\xi_2^{11}}{\partial y_2} = K_n^{II}\Delta^{II}\xi_2^{11} \tag{103}$$

501 It should be noted that there is no displacement along the third direction because of the cleats structure.

502 Combining with the periodic conditions leads to

$$\begin{aligned}\Delta^{I}\xi_1^{11}+\ell\frac{\partial\xi_1^{11}}{\partial y_1} &= 0\\ \Delta^{II}\xi_2^{11}+\ell\frac{\partial\xi_2^{11}}{\partial y_2} &= 0\end{aligned} \tag{104}$$

503 The final solutions are

$$\frac{\partial\xi_1^{11}}{\partial y_1} = -\frac{4\mu(\lambda+\mu)+(\lambda+2\mu)K_n^{II}\ell}{4\mu(\lambda+\mu)+(\lambda+2\mu)(K_n^{I}+K_n^{II})\ell+K_n^{I}K_n^{II}\ell^2} \tag{105}$$

$$\frac{\partial\xi_2^{11}}{\partial y_2} = -\frac{\lambda K_n^{I}\ell}{4\mu(\lambda+\mu)+(\lambda+2\mu)(K_n^{I}+K_n^{II})\ell+K_n^{I}K_n^{II}\ell^2} \tag{106}$$

504 From the definition of the effective stiffness tensor (99), the components $\mathbb{C}^{eff}_{1111}$ and $\mathbb{C}^{eff}_{2211}$ take the form

$$\mathbb{C}^{eff}_{1111} = \frac{K_n^{I}\ell\left[4\mu(\lambda+\mu)+(\lambda+2\mu)K_n^{II}\ell\right]}{4\mu(\lambda+\mu)+(\lambda+2\mu)(K_n^{I}+K_n^{II})\ell+K_n^{I}K_n^{II}\ell^2} \tag{107}$$

$$\mathbb{C}^{eff}_{2211} = \frac{\lambda K_n^{I}K_n^{II}\ell^2}{4\mu(\lambda+\mu)+(\lambda+2\mu)(K_n^{I}+K_n^{II})\ell+K_n^{I}K_n^{II}\ell^2} \tag{108}$$

By proceeding in a similar way, the full solution for the effective stiffness tensor is given as follows

$$
\begin{aligned}
\mathbb{C}^{eff}_{1111} &= \frac{K_n^I \ell \left[4\mu(\lambda+\mu) + (\lambda+2\mu)K_n^{II}\ell\right]}{4\mu(\lambda+\mu) + (\lambda+2\mu)(K_n^I + K_n^{II})\ell + K_n^I K_n^{II}\ell^2} \\
\mathbb{C}^{eff}_{2222} &= \frac{K_n^{II} \ell \left[4\mu(\lambda+\mu) + (\lambda+2\mu)K_n^{I}\ell\right]}{4\mu(\lambda+\mu) + (\lambda+2\mu)(K_n^I + K_n^{II})\ell + K_n^I K_n^{II}\ell^2} \\
\mathbb{C}^{eff}_{3333} &= \lambda + 2\mu - \frac{\lambda^2(4\mu + K_n^I\ell + K_n^{II}\ell)}{\lambda(4\mu + K_n^I\ell + K_n^{II}\ell) + (2\mu + K_n^I\ell)(2\mu + K_n^{II}\ell)} \\
\mathbb{C}^{eff}_{1122} &= \mathbb{C}^{eff}_{2211} = \frac{\lambda K_n^I K_n^{II}\ell^2}{4\mu(\lambda+\mu) + (\lambda+2\mu)(K_n^I + K_n^{II})\ell + K_n^I K_n^{II}\ell^2} \\
\mathbb{C}^{eff}_{1212} &= \frac{\mu K_\tau^I K_\tau^{II}\ell}{\mu(K_\tau^I + K_\tau^{II}) + K_\tau^I K_\tau^{II}\ell} \\
\mathbb{C}^{eff}_{1133} &= \frac{\lambda(2\mu + K_n^{II}\ell)K_n^I\ell}{\lambda(4\mu + K_n^I\ell + K_n^{II}\ell) + (2\mu + K_n^I\ell)(2\mu + K_n^{II}\ell)} \\
\mathbb{C}^{eff}_{2233} &= \frac{\lambda(2\mu + K_n^{I}\ell)K_n^{II}\ell}{\lambda(4\mu + K_n^I\ell + K_n^{II}\ell) + (2\mu + K_n^I\ell)(2\mu + K_n^{II}\ell)} \\
\mathbb{C}^{eff}_{1313} &= \frac{\mu K_\tau^I \ell}{\mu + K_\tau^I \ell} \\
\mathbb{C}^{eff}_{2323} &= \frac{\mu K_\tau^{II} \ell}{\mu + K_\tau^{II} \ell}
\end{aligned}
\tag{109}
$$

C Analytical solution of $\boldsymbol{\eta}$

The problem in $\boldsymbol{\eta}$ for the periodic geometry of cross arrangement shown in Figure 9a can be solved analytically with the given cleat stiffness $\{K_n, K_\tau\}$. Due to the cleat structure inside the cell, there is no deformation according to the third direction, *i.e.* $\epsilon_{33} = 0$.

The stress tensor of matrix phase reads as

$$
\boldsymbol{\sigma}(\boldsymbol{\eta}) = \lambda(\epsilon_{11} + \epsilon_{22}) \begin{pmatrix} 1 & 0 & 0 \\ 0 & 1 & 0 \\ 0 & 0 & 1 \end{pmatrix} + 2\mu \begin{pmatrix} \epsilon_{11} & 0 & 0 \\ 0 & \epsilon_{22} & 0 \\ 0 & 0 & 0 \end{pmatrix}
$$

$$= \begin{pmatrix} (\lambda+2\mu)\epsilon_{11}+\lambda\epsilon_{22} & 0 & 0 \\ 0 & (\lambda+2\mu)\epsilon_{22}+\lambda\epsilon_{11} & 0 \\ 0 & 0 & \lambda(\epsilon_{11}+\epsilon_{22}) \end{pmatrix} \tag{110}$$

511 Noting that the cleats (I) and (II) corresponding to the normal vectors $\mathbf{n}_1^+ = (1,0,0)$ and $\mathbf{n}_2^+ = (0,1,0)$
512 respectively, the interface condition of the closure problem (79) is written as

$$\begin{aligned} \boldsymbol{\sigma}(\boldsymbol{\eta}) \cdot \mathbf{n}_1^+ \cdot \mathbf{n}_1^+ &= K_n^I [\![\eta_n]\!]^I - 1 \\ \boldsymbol{\sigma}(\boldsymbol{\eta}) \cdot \mathbf{n}_2^+ \cdot \mathbf{n}_2^+ &= K_n^{II} [\![\eta_n]\!]^{II} - 1 \end{aligned} \tag{111}$$

513 together with the periodic conditions

$$\begin{aligned} [\![\eta]\!]^I + \epsilon_{11}\ell &= 0 \\ [\![\eta]\!]^{II} + \epsilon_{22}\ell &= 0 \end{aligned} \tag{112}$$

514 The solutions for the jumps of $\boldsymbol{\eta}$ are given by

$$\begin{aligned} [\![\eta]\!]^I &= \frac{\ell\left(2\mu + K_n^{II}\ell\right)}{\lambda\left(4\mu + K_n^I\ell + K_n^{II}\ell\right) + \left(2\mu + K_n^I\ell\right)\left(2\mu + K_n^{II}\ell\right)} \\ [\![\eta]\!]^{II} &= \frac{\ell\left(2\mu + K_n^I\ell\right)}{\lambda\left(4\mu + K_n^I\ell + K_n^{II}\ell\right) + \left(2\mu + K_n^I\ell\right)\left(2\mu + K_n^{II}\ell\right)} \end{aligned} \tag{113}$$

D Biot coefficient for the cleat

Let consider a cleat with an upper normal vector $\mathbf{n}^+$ outward to the matrix. The contact stress in incremental form which is continuous through the cleat is given by

$$\begin{aligned} \mathrm{d}\boldsymbol{\sigma}_f = \mathrm{d}\boldsymbol{\sigma}_m \cdot \mathbf{n}^+ &= K_n[\![\,\mathrm{d}\mathbf{u}_n\,]\!] + K_\tau[\![\,\mathrm{d}\mathbf{u}_\tau\,]\!] - \alpha_f\,\mathrm{d}p_f\,\mathbf{n}^+ \\ &= K_n[\![\,(\mathrm{d}\mathbf{u}\cdot\mathbf{n}^+)\mathbf{n}^+\,]\!] + K_\tau[\![\,\mathrm{d}\mathbf{u} - (\mathrm{d}\mathbf{u}\cdot\mathbf{n}^+)\mathbf{n}^+\,]\!] - \alpha_f\,\mathrm{d}p_f\,\mathbf{n}^+ \end{aligned} \tag{114}$$

where $[\![\,\mathrm{d}\mathbf{u}_n\,]\!]$ and $[\![\,\mathrm{d}\mathbf{u}_\tau\,]\!]$ represent the jump of the displacement in normal and tangential directions through the cleat, α_f the Biot coefficient of the cleat, K_n and K_τ the normal and shear stiffness, which are given by the Bandis and Barton relation

$$\begin{aligned} K_n &= \frac{K_{ni}V_m^2}{(V_m + [\![u_n]\!])^2} \\ K_\tau &= \frac{K_{\tau i}V_m^2}{(V_m + [\![u_n]\!])^2} \end{aligned} \tag{115}$$

with K_{ni}, $K_{\tau i}$ and V_m being the initial normal and shear stiffness and the maximum closure of the cleat when $\boldsymbol{\sigma}_n \to -\infty$.

To determine the Biot coefficient α_f of the cleat, the normal charge P perpendicular to the cleat plane is increased by $\mathrm{d}P$ whereas the fluid pressure in the cleat p_f is increased by $\mathrm{d}p_f$. Since an incremental procedure is performed, the loading can be considered as linear and is split into two distinct steps. In the first step, the fluid remains at pressure p_f and the charge is increased by $\mathrm{d}P - \mathrm{d}p_f$. In the second one, the charge and the fluid pressure are increased both by $\mathrm{d}p_f$. Here, only normal displacement are considered. During the first step according to Bandis-Barton relation, we have

$$-\mathrm{d}(P - p_{f)} = K_n \mathrm{d}[\![u_n^{\mathrm{I}}]\!] \tag{116}$$

During the second step, the stress tensor is uniform both inside the solid and fluid phases and is equal

to $-\mathrm{d}p_f\mathbf{I}$. Therefore the fluid can be replaced by the solid phase. The solid strain tensor is $-\dfrac{\mathrm{d}p_f}{3k_s}\mathbf{I}$ where k_s is the solid bulk modulus. Therefore, the deformation is given by

$$\frac{\mathrm{d}[\![u_n^{\mathrm{II}}]\!]}{V_m + [\![u_n]\!]} = \frac{-\mathrm{d}p_f}{3k_s} \tag{117}$$

The total displacement is the sum of the displacements of the two steps

$$\mathrm{d}[\![u_n]\!] = \mathrm{d}[\![u_n^{\mathrm{I}}]\!] + \mathrm{d}[\![u_n^{\mathrm{II}}]\!] \tag{118}$$

Combining the preceding relations leads to

$$\begin{aligned} -\mathrm{d}P &= K_n\left(\mathrm{d}[\![u_n]\!] + \mathrm{d}p_f\frac{V_m + [\![u_n]\!]}{3k_s}\right) - \mathrm{d}p_f && (119)\\ &= K_n\mathrm{d}[\![u_n]\!] - \underbrace{\left[1 - \frac{K_n}{3k_s}\left(V_m + [\![u_n]\!]\right)\right]}_{\alpha_f}\mathrm{d}p_f && (120)\end{aligned}$$

The Biot coefficient of the cleat is given by

$$\alpha_f = 1 - \frac{K_n}{3k_s}\left(V_m + [\![u_n]\!]\right) = 1 - \frac{K_{ni}V_m - \bar{\sigma}_n^{\mathrm{BB}}}{3k_s} \tag{121}$$

Since $K_{ni}V_m - \bar{\sigma}_n^{\mathrm{BB}} \ll k_s$ for the coal material, it is suitable to assign $\alpha_f = 1$ in numerical simulations.

References

[1] G. Pijaudier–Cabot, J.-M. Pereira, Geomechanics in CO_2 storage facilities, Wiley, 2012.

[2] R. C. Surdam, Geological CO_2 storage characterization, Springer, 2013.

[3] H. Hoteit, M. Fahs, M. R. Soltanian, Assessment of CO_2 injectivity during sequestration in depleted gas reservoirs, Geosciences 9 (2019) 199. doi:doi:10.3390/geosciences9050199.

[4] J. Seidle, Fundamentals of Coalbed Methane Reservoir Engineering, PennWell Corp, 2011.

[5] T. A. Moore, Coalbed methane: A review, International Journal of Coal Geology 101 (2012) 36–81.

[6] H. E. Ross, P. Hagin, M. D. Zoback, CO_2 storage and enhanced coalbed methane recovery: Reservoir characterization and fluid flow simulations of the Big George coal, Powder River Basin, Wyoming, USA, International Journal of Greenhouse Gas Control 3 (2009) 773–786.

[7] H. Kumar, D. Elsworth, J. P. Mathews, J. Liu, D. Pone, Effect of CO_2 injection on heterogeneously permeable coalbed reservoirs, Fuel 135 (2014) 509–521.

[8] G. Wang, K. Wang, Y. Jiang, S. Wang, Reservoir permeability evolution during the process of CO_2 enhanced coalbed methane recovery, Energies 11 (2018) 1–21.

[9] Y. Fan, C. Deng, X. Zhanga, F. Lid, X. Wanga, L. Qiao, Numerical study of CO_2-enhanced coalbed methane recovery, International Journal of Greenhouse Gas Control 76 (2018) 12–23.

[10] J. Ayoub, L. Colson, J. Hinkel, D. Johnston, , J. Levine, Learning to produce coalbed methane, Oilfield Review 3 (1991) 27–40.

[11] Y. Wu, J. Liu, D. Elsworth, Z. Chen, L. Connell, Z. Pan, Dual poroelastic response of a coal seam to CO_2 injection, International Journal of Greenhouse Gas Control 4 (2010) 668–678.

[12] M. Vandamme, L. Brochard, B. Lecampion, O. Coussy, Adsorption and strain: The CO_2-induced swelling of coal, Journal of the Mechanics and Physics of Solids 58 (2010) 1489–1505.

[13] S. Nikoosokhan, M. Vandamme, P. Dangla, A poromechanical model for coal seams injected with carbon dioxide: From an isotherm of adsorption to a swelling of the reservoir, Oil Gas Sci. Technol. Rev. IFP Energies Nouvelles 67 (2012) 777–786.

[14] T. D. Le, Q. D. Ha, I. Panfilov, C. Moyne, Multiscale model for flow and transport in CO_2-enhanced coalbed methane recovery incorporating gas mixture adsorption effects, Advances in Water Resources 144 (2020) 47–60.

[15] T. D. Le, C. Moyne, M. A. Murad, I. Panfilov, A three-scale poromechanical model for swelling porous media incorporating solvation forces: Application to enhanced coalbed methane recovery, Mechanics of Materials 131 (2019) 47–60.

[16] Q. D. Ha, T. D. Le, I. Panfilov, C. Moyne, Solvation force and adsorption isotherm of a fluid mixture in nanopores of complex geometry based on Fundamental Measure Theory, Journal of Physics-Condensed Matter 33 (2021) 335002. doi:{10.1088/1361-648X/ac0ab5}.

[17] S. Nikoosokhan, M. Vandamme, P. Dangla, A poromechanical model for coal seams saturated with binary mixtures of CH_4 and CO_2, Journal of the Mechanics and Physics of Solids 71 (2014) 97–111.

[18] K. Bisdom, G. Bertotti, H. M. Nick, A geometrically based method for predicting stress-induced fracture aperture and flow in discrete fracture networks, AAPG Bulletin 100 (7) (2016) 1075–1097. doi:{10.1306/02111615127}.

[19] S. C. Bandis, A. C. Lumsden, N. R. Barton, Fundamentals of rock joint deformation, International Journal of Rock Mechanics and Mining Sciences & Geomechanics Abstracts 20 (1983) 249–268.

[20] R. E. Goodman, Methods of geological engineering in discontinuous rocks, West Group, 1976.

[21] N. R. Barton, S. C. Bandis, Rock Mechanics and Engineering: Volume 1, CRC Press, 2017, Ch. 1. Characterization and modeling of the shear strength, stiffness and hydraulic behavior of rock joints for engineering purposes, pp. 3–40.

[22] N. R. Barton, Modelling rock joint behavior from in situ block tests: implications for nuclear waste repository design, Technical Report – Office of Nuclear Waste Isolation, ONWI-308, 1982.

[23] J.-L. Auriault, Heterogeneous media: Is an equivalent homogeneous description always possible?, Int. J. Engineering Science 29 (1991) 785–795.

[24] J.-L. Auriault, C. Boutin, C. Geindreau, Homogenization of coupled phenomena in heterogenous media, John Wiley & Sons, 2009.

[25] T. D. Le, M. A. Murad, P. A. Pereira, C. Boutin, Bridging between macroscopic behavior of shale gas reservoirs and confined fluids in nanopores, Computational Geosciences 20 (2016) 751–771.

[26] T. D. Le, M. A. Murad, P. A. Pereira, A new matrix/fracture multiscale coupled model for flow in shale-gas reservoirs, SPE journal 22 (2017) 265–288.

[27] T. D. Le, M. A. Murad, A new multiscale model for flow and transport in unconventional shale oil reservoirs, Applied Mathematical Modelling 64 (2018) 453–479.

[28] F. Bertrand, Hydro-mechanical modelling of multiphase flow in naturally fractured coalbeds applied to CBM recovery or CO2 storage, Ph.D. thesis, Université de Liège, Liège, Belgique (2020).

[29] N. Barton, S. Bandis, K. Bakhtar, Strength, deformation and conductivity coupling of rock joints, International Journal of Rock Mechanics and Mining Sciences & Geomechanics Abstracts 22 (1985) 121–140.

[30] E. Kierlik, M. L. Rosinberg, Density-Functional Theory for inhomogeneous fluids: adsorption of binary-mixtures, Physical Review A 44 (8) (1991) 5025–5037. doi:{10.1103/PhysRevA.44.5025}.

[31] J. S. Barroso, M. A. Murad, P. A. Pereira, A new two-scale computational model for hydromechanical coupling in jointed rocks, Computers & Mathematics with Applications 91 (2021) 67–98.

[32] J. L. Auriault, E. Sanchez-Palencia, Etude du comportement macroscopique d'un milieu poreux saturé déformable, Journal de Mécanique 16 (1977) 575–603.

[33] M. A. Murad, C. Moyne, A dual porosity model for ionic solute transport in expansive clays, Computational Geosciences 12 (2008) 47–82.

[34] S. Torquato, Random heterogeneous materials-microstructure and macroscopic properties, Interdisciplinary Applied Mathematics, 2002.

[35] Z. Pan, L. D. Connell, A theoretical model for gas adsorption-induced coal swelling, International Journal of Coal Geology 69 (4) (2007) 243–252.

[36] F. Bertrand, O. Buzzi, P. Bésuelle, F. Collin, Hydro-mechanical modelling of multiphase flow ins naturally fractured coalbed using a multiscale approach, Journal of Natural Gas Science and Engineering 78 (2020) 103303. doi:10.1016/j.jngse.2020.103303.

Notation

Ω_s : solid domain of the matrix

Ω_n : nanopore domain

Γ_{ns} : nanopore-solid interface

Z : representative unit cell of the matrix

Z_s : solid domain in the unit cell Z

Z_n : nanopore domain in the unit cell Z

∂Z_{ns} : nanopore-solid interface in the unit cell Z

Y : unit cell at microscale

Y_m : matrix domain in the unit cell Y

∂Y_{mf} : matrix-fracture interface in the unit cell Y

$\mathbf{\Pi}$: solvation force vector

p_m : bulk pressure in the matrix

p_f : bulk pressure in the fractures

$\boldsymbol{F}_s$: swelling stress

$\mathbf{u}$: displacement vector

$\mathbf{u}_s$: solid displacement in Z_s

$\mathbf{u}_n$: fluid displacement in Z_n

$\mathbf{u}_m$: matrix displacement in Z_m

$\mathbf{u}_f$: fluid displacement in Z_f

$\mathbb{I}$: fourth-order identity tensor

ϕ_m : porosity of matrix

ϕ_{cleat} : cleats porosity

$\boldsymbol{\alpha}_m$: microscopic Biot-Willis tensor

$\boldsymbol{\alpha}^*_{m,i}$: modified microscopic Biot-Willis tensor

620

$\boldsymbol{\sigma}_s$: solid stress tensor in the solid phase

$\boldsymbol{\sigma}_n$: fluid stress tensor in nanopores

$\boldsymbol{\sigma}_m$: stress tensor in the matrix

$\boldsymbol{\sigma}_f$: stress tensor in the fracture

621

$\mathbf{c}_s$: elastic stiffness tensor of the solid

$\mathbf{C}_m$: effective elastic stiffness tensor of matrix

$\mathbf{C}_m^*$: modified effective elastic stiffness tensor of matrix

$\mathbb{C}^{eff}$: effective elastic stiffness tensor of macroscopic domain